J. Fluid Mech. (1997), *vol.* 334, *pp.* 1–30

Langmuir turbulence in the ocean

By JAMES C. McWILLIAMS[1,2], PETER P. SULLIVAN[2] AND CHIN-HOH MOENG[2]

[1]Atmospheric Sciences Department, Institute of Geophysics and Planetary Physics, UCLA, Los Angeles, CA 90095, USA

[2]National Center for Atmospheric Research, Boulder, Colorado 80307, USA

(Received 29 September 1995 and in revised form 30 September 1996)

Solutions are analysed from large-eddy simulations of the phase-averaged equations for oceanic currents in the surface planetary boundary layer (PBL), where the averaging is over high-frequency surface gravity waves. These equations have additional terms proportional to the Lagrangian Stokes drift of the waves, including vortex and Coriolis forces and tracer advection. For the wind-driven PBL, the turbulent Langmuir number, $La_{tur} = (U_*/U_s)^{1/2}$, measures the relative influences of directly wind-driven shear (with friction velocity U_*) and the Stokes drift U_s. We focus on equilibrium solutions with steady, aligned wind and waves and a realistic $La_{tur} = 0.3$. The mean current has an Eulerian volume transport to the right of the wind and against the Stokes drift. The turbulent vertical fluxes of momentum and tracers are enhanced by the presence of the Stokes drift, as are the turbulent kinetic energy and its dissipation and the skewness of vertical velocity. The dominant coherent structure in the turbulence is a Langmuir cell, which has its strongest vorticity aligned longitudinally (with the wind and waves) and intensified near the surface on the scale of the Stokes drift profile. Associated with this are down-wind surface convergence zones connected to interior circulations whose horizontal divergence axis is rotated about 45° to the right of the wind. The horizontal scale of the Langmuir cells expands with depth, and there are also intense motions on a scale finer than the dominant cells very near the surface. In a turbulent PBL, Langmuir cells have irregular patterns with finite correlation scales in space and time, and they undergo occasional mergers in the vicinity of Y-junctions between convergence zones.

1. Introduction

Mariners and aviators know that the surfaces of lakes and oceans often exhibit arrays of convergence zones, marked by lines of buoyant surface debris. Their usual orientation is roughly parallel to the directions of the surface wind and the primary surface gravity wave propagation, which themselves are usually nearly aligned; we will refer to this direction as longitudinal. These convergence zones are associated with near-surface roll cells, called Langmuir cells, after the early observational characterization by Langmuir (1938). Sub-surface measurements qualitatively confirm the transverse circulation pattern, as well as a longitudinal jet centred in the convergence zone (e.g. Pollard 1977; Weller & Price 1988). Some of the clearest indications of Langmuir cell patterns in the interior come from acoustic scattering off bubbles carried downwards underneath the convergence zones (e.g. Thorpe 1984; Zedel & Farmer 1991; Smith 1992).

The prevailing theoretical interpretation of Langmuir cells is as solutions of the equations derived by Craik & Leibovich (1976), which, in their simplest form, are steady roll cells that are independent of the longitudinal coordinate (x) and periodic in the transverse coordinate (y). The Craik–Leibovich equations are a multi-scale theory for the phase-averaged dynamics of low-frequency motions in the presence of high-frequency surface gravity waves with Stokes drift, a horizontal Lagrangian velocity field $\boldsymbol{u}_s(z)$, where z is height. The essential feature of these dynamics is an added 'vortex force', $\boldsymbol{u}_s \times \boldsymbol{\omega}$ (where $\boldsymbol{\omega} = \nabla \times \boldsymbol{v}$ and $\boldsymbol{v}$ is the low-frequency Eulerian velocity), which is conducive to growth of longitudinal vorticity. For example, in a rapid-distortion solution for weak initial disturbances, with $\boldsymbol{u}_s = \hat{\boldsymbol{x}} u_s$,

$$\boldsymbol{\omega}\,(x - u_s(z)t, y, z, t) = \boldsymbol{\omega}\,(x, y, z, 0) + \hat{\boldsymbol{x}} \frac{\mathrm{d}u_s}{\mathrm{d}z} [\boldsymbol{\omega}\,(x, y, z, 0) \cdot \hat{\boldsymbol{z}}]\, t + O(t^2).$$

This shows that initial seeds of vertical vorticity amplify with time as longitudinal vorticity.

These Langmuir cell solutions occur as the first bifurcation from steady, one-dimensional, longitudinal motion in the non-rotating Craik–Leibovich equations when the laminar Langmuir number,

$$La_{lam} = \left(U_*/U_s Re_s^3\right)^{1/2}, \tag{1.1a}$$

moves below an $O(1)$ threshold value (i.e. an instability of type CL2; see Leibovich 1983). Here U_* is the friction velocity associated with the surface wind forcing ($U_* = (\tau/\rho)^{1/2}$, where τ is the surface stress and ρ is the water density), $U_s = |\boldsymbol{u}_s(0)|$, and Re_s is a Reynolds number based upon U_* and the surface gravity-wave length scale; in this context Re_s is usually assumed to be of $O(1)$ in association with a vertical eddy viscosity representing planetary boundary layer (PBL) turbulence. There are further bifurcations to three-dimensional modes for even smaller La_{lam} (Leibovich & Tandon 1993; Tandon & Leibovich 1995). Li & Garrett (1993, 1995, 1997) examine transient two-dimensional (i.e. x and y) dynamics in the Craik–Leibovich equations for moderate values of La_{lam}, hence behaviour that is effectively laminar. Leibovich (1983) reviews Langmuir cell theory and observations from the perspective of a decade ago.

In nature, however, this phenomenon occurs within the PBL, which usually has fully developed turbulence by the criterion of its Reynolds number being well beyond any marginal stability threshold (e.g. $Re \equiv Uh/\nu = 10^7$ for $U = 0.1$ m s^{-1}, $\nu = 10^{-6}$ m^2 s^{-1}, and $h = 10^2$ m); hence, the PBL also has $La_{lam} \ll 1$. In conventional PBL modelling, the turbulence arises from shear and buoyancy instabilities of the horizontal-mean vertical profiles and transmits the surface fluxes throughout the PBL, and any influences of surface gravity waves are ignored. Such models have had considerable success in matching the observed evolution of PBL profiles (e.g. see the review by Large, McWilliams & Doney 1994).

How can these two apparently unrelated views be reconciled? We attempt to answer this question by solving numerical problems for the oceanic PBL by a large-eddy simulation (LES) that includes the vortex force and other phase-averaged effects associated with the Stokes-drift velocity. Skyllinstad & Denbo (1995) also have recently explored this reconciliation with LES. In this context, where Re is asymptotically large, the relevant parameter measuring the competition between shear instability of the wind-driven currents and the vortex force is a turbulent Langmuir number,

$$La_{tur} = (U_*/U_s)^{1/2}, \tag{1.1b}$$

which empirically is usually around 0.2 to 0.5 under quasi-equilibrium conditions of wind and waves (e.g. Smith 1992). Our preference for LES rather than direct numerical simulation of the Navier–Stokes equations is for the usual geophysical reason of being interested in a larger-Reynolds-number regime than is achievable with the latter (see e.g. Lesieur & Metais 1996).

We refer to the regime of $La_{lam} \ll 1$, $La_{tur} = O(1)$ as Langmuir turbulence, both to associate it with and distinguish it from the laminar Langmuir circulations previously investigated. In the present study we focus on the quasi-equilibrium state as $Re \to \infty$ under the influences of steady, parallel τ and $\boldsymbol{u}_s$, planetary rotation (with Coriolis frequency f), and stable interior stratification that limits the depth of penetration of the PBL (with buoyancy frequency $N = [-(g/\rho_0)(\mathrm{d}\langle\rho\rangle/\mathrm{d}z)]^{1/2}$, with ρ_0 a reference density and the angle brackets a horizontal average). Many previous studies have examined the early-time, two-dimensional transient problem of spin-up from a state of rest, where f can be neglected, with modest Re (Li & Garrett 1993, 1995, 1997). From these it is clear that the presence of Langmuir cells accelerates spin-up and early boundary-layer deepening by enhancement of $\langle uw\rangle$ and $\langle \rho w\rangle$ fluxes in the interior, where (u, v, w) are the (x, y, z) velocity components. In nature, of course, there is often a complex mutual history of surface waves and boundary-layer motions in response to variable winds, hence an enormous variety of scenarios to explore. The quasi-equilibrium state achieved after a time $O(1/f)$ – which we can call the turbulent Stokes–Ekman layer – is a particularly cleanly posed, canonical problem for these Langmuir turbulence dynamics. Our approach here is to establish the existence of Langmuir turbulence in this particular regime and compare its statistical properties and flow structure with another LES solution that is identically posed but for $\boldsymbol{u}_s \equiv 0$. Only a modest exploration of regimes and parameter sensitivities is made here, and the spin-up phase is not analysed.

2. Phase-averaged equations

The Craik–Leibovich equations represent a subset of the full dynamics of interacting surface gravity waves and PBL turbulence. The result of the low-pass time (or wave-phase) averaging applied to the full Navier–Stokes equations is the reduced set of Craik–Leibovich equations that describes fluid motions in the oceanic PBL for a flat water surface (the rigid lid approximation for dynamics excluding surface gravity waves). The sole effect of the surface waves enters through the Stokes drift associated with the waves. Thus, any modification of the wave field by the evolving turbulence field is neglected.

We will obtain solutions of the Craik–Leibovich equations by LES. These include augmentation of the LES Navier–Stokes equations by a generalized vortex force, $\boldsymbol{u}_s \times [f\hat{\boldsymbol{z}} + \boldsymbol{\omega}]$, and an additional advection of any material property P by the wave-induced Lagrangian motion, $\boldsymbol{u}_s \cdot \nabla P$. Following the original Craik–Leibovich derivation for a uniform-density fluid in a non-rotating environment, more general and more elegant derivations of these equations have since been made as either a generalized Lagrangian wave/mean-flow theory (Leibovich 1980; Craik 1985) or an averaged Hamilton's principle (Holm 1996).

A LES model is formally based upon a filtering of the fundamental fluid equations of motion. In most applications the filter is simply a low-pass spatial one, but to include the vortex force here it must also be a temporal filter that averages over the irrotational surface gravity waves. The LES formulation is essentially that of Moeng (1984) with a modified sub-grid-scale model (SGS) in the surface layer to improve

correspondences with Monin–Obukhov similarity theory (Sullivan, McWilliams & Moeng 1994), an altered surface boundary condition for momentum (i.e. replacing the solid-boundary no-slip condition with specified stress; McWilliams *et al.* 1993), and an internal-gravity-wave radiation boundary condition in the stratified interior (Klemp & Duran 1983). It is arguable that the SGS model also ought to be modified due to the presence of $\boldsymbol{u}_s$, but we have not done so; excuses for this are the somewhat *ad hoc* basis for SGS models in general, hence our uncertainty about how to include Stokes effects, and our experience that LES PBL solutions are often not sensitive to the details of the SGS formulation.

The filtered (i.e. LES) Craik–Leibovich equations are

$$\frac{\mathrm{D}\boldsymbol{v}}{\mathrm{D}t} + f\hat{\boldsymbol{z}} \times (\boldsymbol{v} + \boldsymbol{u}_s) = -\nabla\pi - g\hat{\boldsymbol{z}}(\rho/\rho_0) + \boldsymbol{u}_s \times \boldsymbol{\omega} + SGS, \tag{2.1}$$

$$\frac{\mathrm{D}\rho}{\mathrm{D}t} + \boldsymbol{u}_s \cdot \nabla\rho = SGS, \tag{2.2}$$

$$\nabla \cdot \boldsymbol{v} = 0. \tag{2.3}$$

We have indicated the SGS terms only schematically; g is the gravitational acceleration, $\mathrm{D}/\mathrm{D}t = \partial_t + \boldsymbol{v} \cdot \nabla$, and π is a generalized pressure,

$$\pi = p/\rho_0 + \left(\tfrac{1}{2}\right)\left[|\boldsymbol{v} + \boldsymbol{u}_s|^2 - |\boldsymbol{v}|^2\right].$$

We assume a trivial equation of state where the density is proportional to the temperature θ, hence to the internal energy; i.e. $\rho = \rho_0(1 - \alpha\theta)$, where α is the thermal expansion coefficient. Skyllingstad & Denbo (1995; hereafter SD95) have recently reported analogous LES Langmuir turbulence solutions for an intermediate fluid model that does not include the Coriolis vortex force in (2.1) proportional to Stokes drift; consequently, we find both similarities and differences between their solution properties and ours as described below.

For simplicity, we assume the surface gravity wave field is a steady, monochromatic, deep-water wave propagating in the $+\hat{\boldsymbol{x}}$ direction. Its solution form for surface elevation, to leading order in wave steepness (ak), is

$$\eta = a\cos[kx - \sigma t],$$

and the associated Stokes drift is

$$\boldsymbol{u}_s = \hat{\boldsymbol{x}}\, U_s \mathrm{e}^{2kz}, \tag{2.4}$$

where $z = 0$ is the average surface height, a is the wave amplitude, k is the wavenumber, $U_s = \sigma k a^2$, and $\sigma = (gk)^{1/2}$ (Phillips 1977). In nature, of course, the wave field would have a broad-band spectrum, and $\boldsymbol{u}_s$ consequently would have a more complex vertical profile. We do not expect this to make an important qualitative difference to the Langmuir turbulence solutions, based on some exploratory solutions (not reported here). Of far greater importance, perhaps, is the neglect of more nonlinear aspects of surface gravity wave dynamics, especially wave breaking which causes increased mixing and dissipation near the surface.

3. The laminar Stokes–Ekman layer

Before examining turbulent LES solutions of (2.1)–(2.4), we first consider the simpler case of the Craik–Leibovich equations for the classical Ekman boundary layer

problem in a uniformly rotating, uniform-density fluid. The horizontally averaged, linear momentum equations are

$$u_t - f(v + v_s) = -F^x_z, \quad v_t + f(u + u_s) = -F^y_z, \tag{3.1}$$

after subtraction of a mean geostrophic, hydrostatic balance that is assumed to have no boundary-layer structure. Here $\boldsymbol{F} = (F^x, F^y)$ is the turbulent vertical flux of horizontal momentum. We further specialize the problem to having both the surface wind stress and the Stokes drift oriented in the $+\hat{\boldsymbol{x}}$ direction. Thus, $\tau > 0$, $v_s = 0$, $u_s(z) \geqslant 0$, and the boundary conditions for (3.1) are

$$\left.\begin{array}{l} F^x = -\tau/\rho, \ F^y = 0 \ \text{ at } \ z = 0, \\ u, v, F^x, F^y \to 0 \ \text{ as } \ z \to -\infty. \end{array}\right\} \tag{3.2}$$

We assume the Stokes drift is as in (2.4).

Integral momentum budgets for (3.1)–(3.2) are

$$S_t - fT = \frac{\tau}{\rho}, \quad T_t + fS = -\frac{fU_s}{2k}, \tag{3.3}$$

for the Eulerian horizontal volume transport,

$$(S, T) \equiv \int_{-\infty}^{0} (u, v)\, \mathrm{d}z. \tag{3.4}$$

Thus, the horizontal transport in steady-state balance has the familiar wind-driven Ekman component perpendicular to the wind (i.e. $T < 0$ for $f > 0$ in the northern hemisphere) plus an additional up-wave component ($S = -U_s/2k < 0$) that cancels the Stokes-drift transport (i.e. $\int u_s\, \mathrm{d}z = +U_s/2k$). Additionally one can superimpose on the steady solution an inertial oscillation, assuming that it satisfies the boundary conditions in (3.2).

To examine boundary-layer profiles, we assume an eddy viscosity relation,

$$\boldsymbol{F} = -\nu \boldsymbol{v}_z, \tag{3.5}$$

to close the problem (3.1)–(3.2) in a way that is equivalent to making the flow laminar; this problem was first considered by Huang (1979). The solution is easiest to manipulate if we define a complex variable $U = u + \mathrm{i}v$, for which the problem is

$$\left.\begin{array}{l} U_t + \mathrm{i}fU - \nu U_{zz} = -\mathrm{i}fU_s \mathrm{e}^{2kz}, \\ \nu U_z = \tau/\rho \ \text{ at } \ z = 0, \\ U \to 0 \ \text{ as } \ z \to -\infty. \end{array}\right\} \tag{3.6}$$

The steady-state solution is

$$U = \frac{1 - \mathrm{i}}{(2f\nu)^{1/2}}[\tau/\rho - 2k\nu\gamma] \exp\left[\frac{1 + \mathrm{i}}{\sqrt{2}} \left(\frac{f}{\nu}\right)^{1/2} z\right] + \gamma \mathrm{e}^{2kz}, \tag{3.7}$$

where $\gamma = \mathrm{i}fU_s[4k^2\nu - \mathrm{i}f]^{-1}$.

To simplify the interpretation of (3.7), we non-dimensionalize variables by the wind-driven scales,

$$U, \boldsymbol{v}, \boldsymbol{u}_s \sim \frac{\tau}{\rho(2f\nu)^{1/2}}, \quad z \sim (2\nu/f)^{1/2},$$

and furthermore define a non-dimensional amplitude and vertical wavenumber for the Stokes-driven component by $s = U_s\rho(2f\nu)^{1/2}\tau > 0$ and $r = k(2\nu/f)^{1/2} > 0$. Then

the non-dimensional solution is

$$U(r,s,z) = (1-\mathrm{i})(1-r\hat{\gamma})\mathrm{e}^{(1+\mathrm{i})z} + \hat{\gamma}\mathrm{e}^{2rz}, \tag{3.8}$$

where

$$\hat{\gamma} = \frac{-1+\mathrm{i}2r^2}{1+4r^4}s. \tag{3.9}$$

The transport integral for (3.8), matching (3.3) in steady state, is $-s/2r - \mathrm{i}$, oriented obtusely to the right of the wind and waves. The vertical profile has a clockwise spiral component that decays on the Ekman scale and a rectilinear component, oriented obtusely to the left of the wind and waves, that decays on the scale of the Stokes drift.

The surface current in (3.8) is

$$u(0) \;=\; 1 + s\frac{-1+r-2r^3}{1+4r^4}, \quad v(0) \;=\; -1 + s\frac{-r+2r^2-2r^3}{1+4r^4}. \tag{3.10}$$

This velocity is oriented 45° to the right of the wind when $s = 0$. The surface velocity component proportional to s has a zonal value of -1 for $r \to 0$, changes sign at $r \approx 0.59$, achieves a maximum of ≈ 0.4 at $r \approx 1.1$, and vanishes as $r \to \infty$. Its meridional value is always negative and thus reinforces the sense of the wind-driven flow, vanishes as $r \to 0, \infty$, and has a minimum of ≈ -0.21 at $r \approx 0.7$. For all $s > 0$, the surface current is oriented farther away from the wind than in the pure Ekman layer.

Even in the limit of vanishing wind stress (i.e. $s \to \infty$ in (3.9)), there is a boundary-layer current with zero surface stress and westward transport:

$$U = \hat{\gamma}\left(r[-1+\mathrm{i}]\mathrm{e}^{(1+\mathrm{i})z} + \mathrm{e}^{2rz}\right). \tag{3.11}$$

Its hodograph exhibits a clockwise spiral, with two vertical decay scales, starting with a southward surface component. If we simultaneously take the limit of vanishing eddy viscosity (i.e. $r \to 0$), then $U \to -s$ everywhere except at $z = 0$; here the Eulerian flow cancels the Stokes drift except to accommodate the surface boundary condition of zero stress (see also §8).

Lagrangian parcels in the Stokes–Ekman layer move with $\boldsymbol{v} + \boldsymbol{u}_s$; this is the trajectory that a tracer or a drifting buoy follows. Thus, since S is the opposite of the Stokes-drift vertical integral, the boundary-layer Lagrangian transport is $\hat{\mathbf{y}}T$ (the same as in the pure Ekman layer), and the Lagrangian surface current has a greater magnitude and is directed more towards the wind for all values of $s, r > 0$.

To have some sense of the relative contributions of the wind and wave components of the solution, consider the following representative example (which also matches the turbulent problem posed in §4). We choose $\tau = 0.037$ N m^{-2}, corresponding to a wind speed of about 5 m s^{-1}; thus, the value of the friction velocity is $U_* = 6.1 \times 10^{-3}$ m s^{-1}. We also choose $f = 10^{-4}$ s^{-1}, $k = 2\pi/60 = 0.105$ m^{-1}, and $U_s = 0.068$ m s^{-1} (corresponding to a wave amplitude of 0.8 m). This implies a turbulent Langmuir number, $La_{tur} = (U_*/U_s)^{1/2}$ of 0.3. Finally, we identify the Ekman-layer e-folding scale $(2\nu/f)^{1/2}$ with $h_e = 0.25U_*/f$ (Coleman, Ferziger & Spalart 1990); hence, $\nu = 1.16 \times 10^{-2}$ m^2 s^{-1} and the e-folding scale is 15 m. Thus, the non-dimensional wave parameters in (3.8)–(3.9) are $s = 2.79$, $r = 1.60$, and $\hat{\gamma} = -0.10 + 0.52\mathrm{i}$, which implies the substantial Stokes-drift modifications of the wind-driven Ekman layer (figure 1): the Stokes–Ekman Eulerian ($\boldsymbol{v}$) and Lagrangian ($\boldsymbol{v} + \mathbf{u}_s$) mean surface currents are to the south and east-southeast, respectively, compared to the southeast

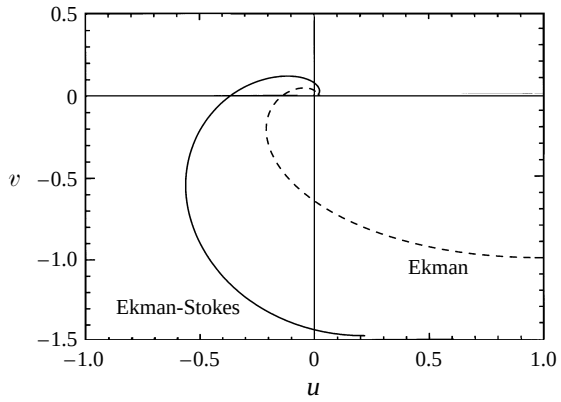

FIGURE 1. Hodograph of the laminar Stokes–Ekman layer (solid line) from (3.7) for $s = 2.79$ and $r = 1.6$ (see text); also shown is the Ekman hodograph, $s = 0$ (dashed line).

direction of the Ekman surface current. For higher or longer surface waves, or weaker winds, the wave-driven modifications would be relatively larger.

4. Posing the Langmuir turbulence problem

We consider a domain that is rectangular in three dimensions. The boundary conditions are the following: horizontal periodicity, outward wave radiation and zero stress at the bottom, and no-normal flow and specified momentum and density (temperature) fluxes at the top.

We choose the wind and wave fields to be aligned in the direction $+\hat{\boldsymbol{x}}$, with $\tau = 0.037$ N m^{-2} (corresponding to a wind speed of about 5 m s^{-1}) and assume it is constant in time. Thus, the value of the friction velocity is $U_* = 6.1 \times 10^{-3}$ m s^{-1}. The wave Stokes drift is as in (2.4). We have obtained solutions for a variety of (a, k) values, but we will focus primarily on the set (0.8 m, $2\pi/60 = 0.105$ m^{-1}), which corresponds to $U_s = 0.068$ m s^{-1} and $La_{tur} = 0.3$. We demonstrate the behaviour of Langmuir turbulence by comparing it with an identically posed problem without $\boldsymbol{u}_s$, which we designate shear turbulence.

The boundary layer environment is uniformly rotating, with $f = 10^{-4}$ s^{-1}, corresponding to 45° N latitude. Thus, the value of the turbulent Ekman-layer depth scale is $h_e = 0.25U_*/f_0 = 15$ m. It is also bounded by a stably stratified layer below. The initial stability profile is neutral for $0 \geqslant z > -z_i$, with $z_i = 33$ m, and has a uniform $N = 0.0044$ s^{-1} below, corresponding to $\mathrm{d}\theta/\mathrm{d}z = 0.01$ K m^{-1} and $\alpha = 2 \times 10^{-4}$ K^{-1}. Since $z_i \sim h_e$, the profiles of PBL motions are compressed somewhat by the interior stratification (McWilliams *et al.* 1993). Even this relatively weak stratification suffices to make the rate of PBL deepening by entrainment small ($O(1)$ m day^{-1}) over integration periods of $O(1/f) \sim 3$ hrs that reach a quasi-equilibrium state with respect to the wind- and wave-driving. In this regime, a large-eddy turnover time is $O(z_i/U_*) \sim 1.5$ hrs. We also include a heat flux into the ocean of $Q_* = -5$ W m^{-2}, which implies a Monin–Obukhov length of $L = \rho_0 c_p U_*^3/\kappa\alpha g Q_* = -240$ m (where κ is von Kármán's constant and c_p is the heat capacity). Thus, $z_i/L \approx -0.14$ is small, and this is a weakly convective, strongly sheared PBL regime. Similarly, the Hoenikker number, $Ho = -2\alpha g Q_*/\rho_0 c_p k U_s U_*^2 \approx 0.02$, is also small (Li & Garrett 1995), indicating that the convective forcing of Langmuir cells is less than that as-

sociated with the Stokes drift vortex force. We include $Q_* \neq 0$ only to facilitate the spin-up from rest. Such solutions do contain inertial oscillations, whose spatial structure is horizontally and vertically uniform down to $z = z_i$ and nearly zero below. These oscillations are effectively decoupled from the quasi-equilibrium PBL dynamics, as demonstrated by comparing turbulence statistics in different inertial phases, and they are ignored (removed by time averaging) in the statistical analyses below. LES involves a sub-grid-scale eddy viscosity ν_{sgs} (Moeng 1984). In our solutions we find that $\nu_{sgs} = O(10^{-3})$ m^2 s^{-1}, which is much larger than the molecular viscosity; nevertheless, even if we use ν_{sgs} to calculate an effective La_{lam} from (1.1*a*), its value is $O(10^{-3}) \ll La_{tur}$, which assures that La_{tur} is indeed the relevant measure for our LES solutions.

Based upon the values of k^{-1}, h_e, and z_i above, we choose a domain depth of $H = 90$ m, well below the PBL bottom at $z = -z_i$. Based upon the expectation from laminar Craik–Leibovich solutions that Langmuir cells have a moderately anisotropic aspect ratio, we choose the standard (S) horizontal dimensions to be $L_x = L_y = 150$ m with a grid of $50 \times 50 \times 150$, which implies resolution scales of $\Delta x = \Delta y = 3$ m and $\Delta z = 0.6$ m. For some calculations, to test the constraint of the finite horizontal extent, we also use an extended (E) domain of $L_x = L_y = 300$ m and grid of 64×64, hence $\Delta x = \Delta y = 4.7$ m. We also have calculated solutions in the extended domain with a nested grid (N) in the top 9 m near the surface, with horizontal and vertical resolution scales of 1.2 and 0.3 m, respectively (see Sullivan, McWilliams & Moeng 1996). We will analyse these alternative solutions for Langmuir turbulence with different trade-offs in resolution and domain size; comparing them gives an indication of the discretization errors in the calculations and sampling errors in calculating the averages.

5. Low-order statistics of Langmuir turbulence

We begin our analysis of Langmuir turbulence by comparing its low-order statistical moments with those of an identically posed problem for shear turbulence. These moments are based on averages, denoted by angle brackets, over the horizontal domain and over many large-eddy turnover times during the quasi-equilibrium phase following a spin-up from rest. The moments include vertical profiles of mean, variance, covariance, and skewness for various flow properties, which are the usual statistical measures of PBL turbulence. We denote a particular solution by a label in the form 'domain/La_{tur}', and the other parameters specified above are implicit; thus, shear turbulence in the standard domain is labelled S/∞, and Langmuir turbulence in the extended domain is E/0.3.

The mean horizontal velocity is shown in figure 2. The largest difference between Langmuir turbulence and shear turbulence is in $\langle u \rangle(z)$: in Langmuir turbulence (but not shear turbulence) it has a negative value for both the surface value and transport. It is also much more uniformly distributed with depth in Langmuir turbulence, indicating the presence of a more efficient vertical transport process than in shear turbulence, which we can anticipate to be the Langmuir cells. This is true in general for the turbulent boundary layers: both shear turbulence and Langmuir turbulence exhibit less spiral in their hodograph than their laminar counterparts. The differences in $\langle v \rangle(z)$ are more modest between Langmuir turbulence and shear turbulence. In both cases the tangential flow component is to the south, but the depth distribution is again more uniform in Langmuir turbulence. Compared to the laminar boundary layer (§3 and figure 1), all mean surface current directions are shifted in

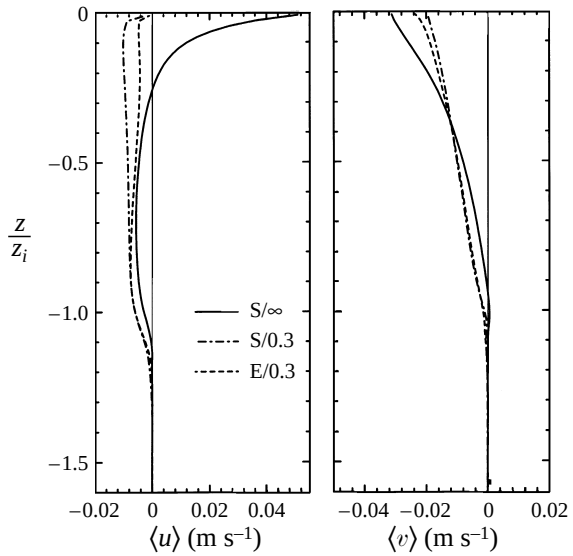

FIGURE 2. Horizontal and time-mean horizontal velocity profiles, $\langle u \rangle(z)$, $\langle v \rangle(z)$. Included are one solution for shear turbulence (S/∞) and two for Langmuir turbulence (S/0.3 and E/0.3).

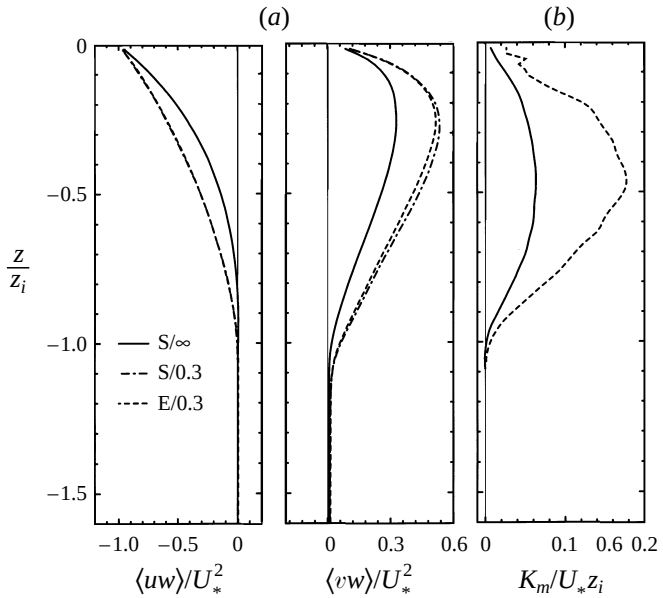

FIGURE 3. (*a*) Mean vertical momentum flux profiles, $\langle u'w \rangle(z)$, $\langle v'w \rangle(z)$, normalized by the surface momentum flux U_*^2. (*b*) Bulk eddy viscosity profiles, $-\langle \boldsymbol{v}'w \rangle \cdot \langle \boldsymbol{u}_z \rangle / \langle \boldsymbol{u}_z^2 \rangle$, normalized by $U_* z_i$.

the counterclockwise direction in the turbulent solutions, but the mutual relations for the orientation between Langmuir turbulence and shear turbulence and between Eulerian and Lagrangian are all qualitatively the same. Weller & Price (1988, figures 13–14) observed that the mean surface flow is often nearly perpendicular to the wind direction when Langmuir cells are present, consistent with the southward flow here, although the observational testing of this prediction is not yet very precise. This

mean flow behaviour is missing in the SD95 solutions because they did not include the Stokes Coriolis force in their equations.

We also see modest differences in the two Langmuir turbulence solutions (S/0.3 and E/0.3) in figure 2, the greater part of which is sampling error in filtering out the inertial current, whose magnitude is comparable to the mean current. Other statistical moments shown below have no contribution from horizontal mean quantities, and they show much closer correspondences between the two Langmuir turbulence solutions. Thus, the computational and analysis errors here are generally small enough to allow firm conclusions about the differences between Langmuir turbulence and shear turbulence.

Profiles of the mean vertical flux of horizontal momentum are shown in figure 3(*a*). These, of course, are strongly constrained by the imposed surface stress and the mean velocity profiles (figure 2) through the mean horizontal momentum balance ((3.1) in steady state). They are qualitatively similar in Langmuir turbulence and shear turbulence, although Langmuir turbulence has a significantly larger magnitude in the interior of the PBL, hence again a greater transport efficiency. This is confirmed by having a bulk eddy viscosity (i.e. $K_m(z) \equiv -\langle \boldsymbol{v}'w \rangle \cdot \langle \boldsymbol{u}_z \rangle / \langle \boldsymbol{u}_z^2 \rangle$) about three times larger in Langmuir turbulence than in shear turbulence (figure 3*b*). The bulk eddy viscosities in figure 3(*b*) have magnitudes on the order of $0.1 U_* z_i = 2 \times 10^{-2}$ m^2 s^{-1}, which exceeds ν_{sgs} by more than an order of magnitude. They also have the convex profile shape that is assumed in the K-profile parameterization for turbulent transports in shear- and buoyancy-driven PBLs (Large *et al*., 1994), suggesting that Langmuir turbulence might be similarly parameterized but with an enhanced transport coefficient compared to shear turbulence. This convex eddy-viscosity profile differs strongly from that proposed by SD95 (their equation (9) and figure 3).

Also discernible in figure 3(*a*) is a relatively weak $\langle v'w \rangle > 0$ and $\langle u'w \rangle = 0$ beneath the PBL. The flux is nearly constant with depth, implying no contribution to the mean momentum balance, hence no necessity for a balancing mean velocity in the Coriolis force in (3.1). (This depth range also has u_s nearly zero.) This flux is carried by internal gravity waves radiating downward out the bottom of the domain. The waves are generated in the entrainment layer by the interaction of PBL turbulence with the stable mean stratification by a process that is not quantitatively well understood (nor accurately calculated with typical LES grid resolution). Other measures of the sub-PBL waves can be seen in figures 4–9 below. Their amplitude is somewhat larger in Langmuir turbulence compared to shear turbulence, probably because the PBL turbulent variances (below) are larger in Langmuir turbulence. Previous examples of internal-wave generation by PBL turbulence are in Carruthers & Moeng (1987) and Fernando (1991).

Eddy kinetic energy is larger in Langmuir turbulence than shear turbulence, especially within the top few metres (figure 4), as is also observed in laboratory Langmuir turbulence (Magnaudet & Thais 1995). Although the SGS kinetic energy is also larger in Langmuir turbulence, it makes up a smaller fraction of the total, which suggests that it is exerting a lesser degree of dynamical control over the resolved-scale fluid dynamics in the Langmuir turbulence LES solution.

The mean budget equation for resolved-scale eddy kinetic energy can be derived from (2.1), assuming equilibrium; it is

$$\frac{\partial \frac{1}{2} \boldsymbol{v}'^2}{\partial t} = 0 = -\frac{\partial \langle \boldsymbol{v}'^2 w \rangle}{\partial z} - \langle \boldsymbol{v}'w \rangle \cdot \frac{\partial \langle \boldsymbol{v} \rangle}{\partial z} + \alpha g \langle \theta' w \rangle - \frac{1}{\rho_0} \frac{\partial \langle p'w \rangle}{\partial z} - \langle u'w \rangle \frac{\partial u_s}{\partial z} - \epsilon, \quad (5.1)$$

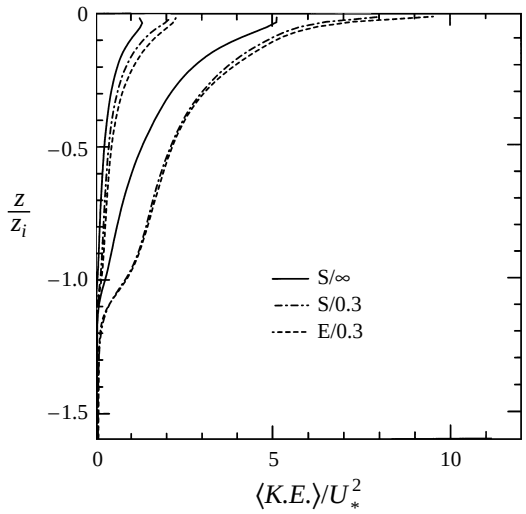

FIGURE 4. Mean eddy kinetic energy profiles, $\langle \boldsymbol{v}'^2 \rangle(z)$, normalized by U_*^2. Separate groups of curves are for the SGS component and the total.

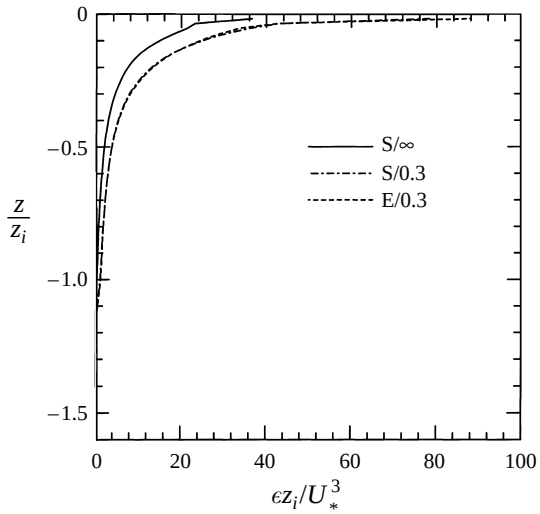

FIGURE 5. Mean kinetic energy dissipation profiles, $\epsilon(z)$, normalized by $U_*^3/z_i \approx 7 \times 10^{-9}$ m^2 s^{-3}. (See Moeng 1984 for definition.)

where the prime denotes a departure from horizontal average. The terms in (5.1) are referred to, respectively, as transport, shear production, buoyancy production, pressure working, 'Stokes production', and dissipation. (Equation (5.1) differs in its Stokes production term from the eddy kinetic energy budget of SD95 (their Appendix) because they failed to include the Stokes term in the generalized pressure in (2.1).) In the present LES solutions, transport and buoyancy production are relatively small contributors to this budget. In shear turbulence, the pressure working is also relatively small, and shear production approximately balances dissipation at all depths. In Langmuir turbulence, however, Stokes production adds greatly to shear production and combines with pressure working to increase eddy kinetic energy, collectively

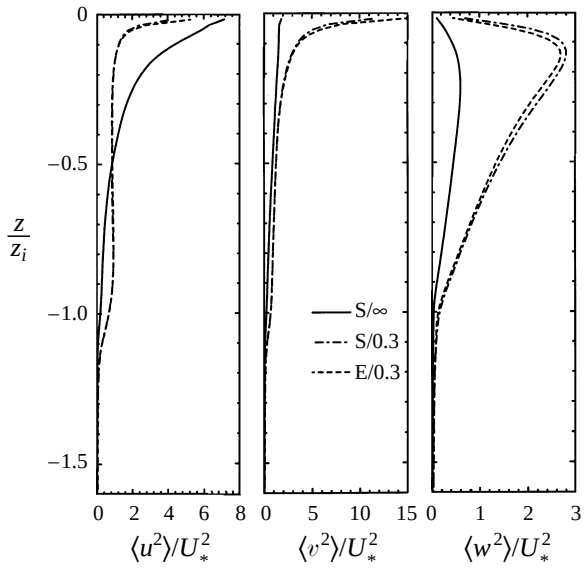

FIGURE 6. Mean velocity variance profiles for the resolved motion, $\langle u'^2\rangle(z)$, $\langle v'^2\rangle(z)$, and $\langle w'^2\rangle(z)$, normalized by U_*^2.

balanced against dissipation. Thus, the dissipation $\epsilon(z)$ is much larger in Langmuir turbulence than in shear turbulence (figure 5). While budget contributions do not rigorously imply causality, this behaviour suggests why eddy kinetic energy is so much larger in Langmuir turbulence. A similar analysis has been made for the covariance budgets of mean momentum and buoyancy fluxes, but the interpretation is somewhat more ambiguous since the analogous added Stokes production is largely cancelled by increased pressure working; however, if one argues that the latter, as an isotropizing influence (Rotta 1951; Wyngaard, Cote & Izumi 1971), acts like additional damping or dissipation for the intrinsically anisotropic motions that sustain the fluxes, then their interpretation is also analogous. The dissipation profile in figure 5 is very strongly peaked near the surface, even without any benefit of enhanced dissipation by surface gravity-wave breaking. It reaches a magnitude of nearly 10^{-6} m^2 s^{-3} (after multiplication by the normalization factor $U_*^3/z_i = 7 \times 10^{-9}$ m^2 s^{-3}). This magnitude is similar to those observed by Anis & Moum (1992) and modelled in the Langmuir turbulence solution of SD95 (their figures 6 and 7), using the conversion factor $\propto U_*^3$ to match their stronger wind-stress conditions.

Langmuir turbulence has much greater velocity anisotropy than shear turbulence, as shown in the component variances (figure 6). The larger transverse and vertical motions and weaker longitudinal motions (except very near the surface) in Langmuir turbulence are as would be expected from the presence of transverse Langmuir cells instead of the more isotropic turbulent eddies in shear turbulence. Note that the horizontal velocity variances are strongly surface intensified in Langmuir turbulence, roughly on the e-folding scale of the Stokes drift (2.4), whereas the vertical velocity variance remains large throughout the PBL, indicating that the Langmuir cells fill the weakly stratified layer, $0 \geqslant z \geqslant -z_i$. Together these profiles indicate the presence of at least two vertical scales for the Langmuir cells in Langmuir turbulence.

The negative skewness of the vertical velocity (figure 7) indicates that downward motions are narrower and stronger than the broader upward motions required for

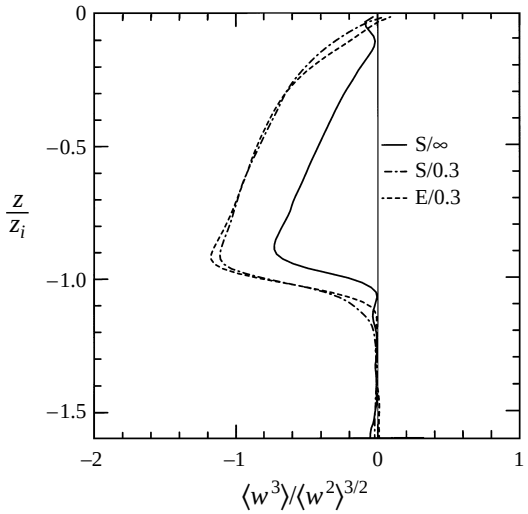

FIGURE 7. Mean vertical velocity skewness profiles.

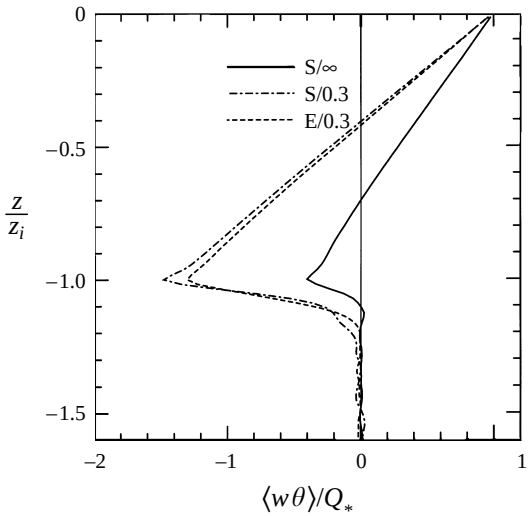

FIGURE 8. Mean heat flux profiles, $\langle \theta w \rangle(z)$ normalized by the surface heat flux Q_*.

net mass balance. The skewness magnitude is greater for Langmuir turbulence than shear turbulence, although less so than in some previous two-dimensional laminar Craik–Leibovich solutions (e.g. Li & Garrett 1993) or in Pollard's (1977) often-cited sketch based on velocity observations. The skewness grows monotonically with depth through the PBL and is largest near $z = -z_i$ in both Langmuir turbulence and shear turbulence. Thus, downward vertical velocity pulses, driven from the top surface by instability of the mean velocity profile, extend appreciably into the entrainment layer.

The mean buoyancy flux profiles (figure 8) show much larger entrainment rates for Langmuir turbulence than shear turbulence, as was also shown in Li, Zahariev & Garrett (1995). (The two flux profiles must coincide at the upper surface to match the imposed surface buoyancy flux.) There is also a significantly larger eddy diffusivity throughout the boundary layer in Langmuir turbulence, analogous to the

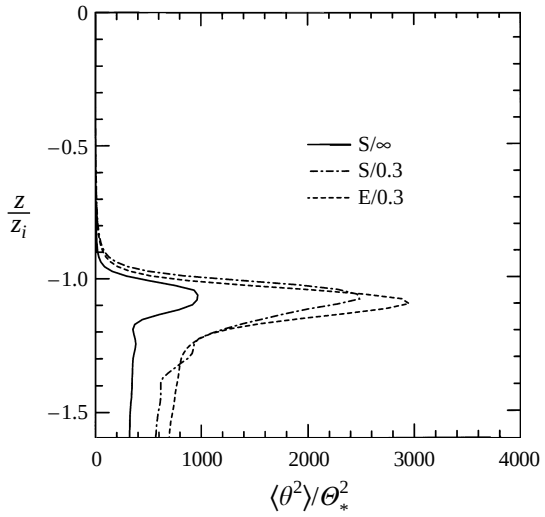

FIGURE 9. Mean temperature variance profiles, $\langle\theta'^2\rangle(z)$, normalized with a temperature scale $\Theta_* = -Q_*/U_* \approx 2 \times 10^{-4}$ K.

eddy-viscosity enhancement in figure 3(*b*), although the former has singularities in the middle of the PBL and is thus a less useful diagnostic measure than the latter. Because of the larger buoyancy flux minimum in the entrainment layer, the average rate of boundary layer deepening, $W_e \equiv \mathrm{d}z_i/\mathrm{d}t$, is also much greater in Langmuir turbulence than in shear turbulence (i.e. $W_e/U_* \approx 6.0$ and 2.6×10^{-3}, respectively). The enhanced buoyancy-transport efficiency in Langmuir turbulence is consistent with its greater turbulent kinetic energy (figure 4) and vertical velocity down-draught bias (figure 7). Consequently, the temperature variance is also enhanced in Langmuir turbulence (figure 9), both in the entrainment layer and in association with the internal gravity waves beneath the PBL. The Langmuir turbulence solutions of SD95 (their figure 4) also show an enhanced entrainment-layer heat flux, albeit to a lesser degree than in figure 8, consistent with their relatively larger Q_* (with *Ho* values 3–10 times larger) that diminishes the relative contribution by Langmuir cells.

6. Flow structures in Langmuir turbulence

Now we examine the patterns of the currents in Langmuir turbulence. Since many observations are of material distributions near the surface (surfactants and bubbles), we calculate Lagrangian trajectories for surface-trapped objects. The evolutionary equation is

$$\frac{\mathrm{d}\boldsymbol{X}}{\mathrm{d}t} = \boldsymbol{v}(\boldsymbol{X}, 0, t) + \boldsymbol{u}_s(\boldsymbol{X}, 0, t), \quad \boldsymbol{X}(0) = \boldsymbol{X}_0, \tag{6.1}$$

where $\boldsymbol{X}(t) \equiv (X, Y, 0)$ is the horizontal parcel coordinate. One realization is shown in figure 10(*a*) for an array of $\boldsymbol{X}(t)$ released along a line of constant X_0 at the surface. The overall parcel motion is to the east-southeast, as in the laminar Stokes–Ekman layer (§3), at an average speed of about 0.1 m s^{-1}, which is the mean of the right-hand side of (6.1). Convergence zones are clearly seen, and few parcels remain outside them. The zones are extremely narrow in most places, although some sectors have an apparently finite width in which nearby parcels move in parallel with each other along

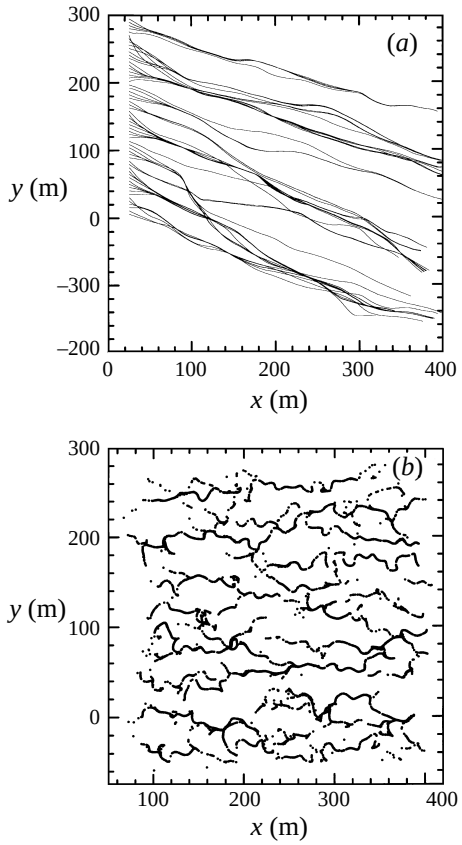

FIGURE 10. (*a*) Trajectories of 60 surface parcels released along a transverse line over an interval of 5920 s in Langmuir turbulence solution E/0.3; (*b*) Locations of 10^4 surface parcels 1440 s after being released randomly within $0 \leqslant x, y \leqslant 300$ m.

the zone axis. A typical spacing between the zones is about 50 m, which is roughly the surface gravity wavelength $2\pi/k = 60$ m. However, there is evident irregularity in these zones: they are wobbly, their spacing is irregular, and parcels occasionally escape. There are also instances of zones joining, which is indicative of the Langmuir cell merger seen in two-dimensional laminar solutions (Li & Garrett 1993) and Y-junctions seen in time-range acoustic scattering patterns (Thorpe 1992; Farmer & Li 1995). In figure 10(*b*) is shown the instantaneous distribution of 10^4 surface parcels at a little more than one-quarter of an eddy turnover time after being released randomly throughout the domain. They too have aggregated into convergence zones that occupy a small fraction of the domain. However, in comparison with the trajectory view of figure 10(*a*), this synoptic view has a somewhat more fractured pattern whose dominant orientation is more longitudinal. Our impression is that the Langmuir cell patterns in our Langmuir turbulence solutions are about as well organized as those observed, but this needs to be quantitatively assessed.

An instantaneous Eulerian depiction of the Langmuir cell pattern is provided by the longitudinal vorticity in three dimensions (figure 11*a*). It shows irregularly spaced, longitudinally elongated, tangentially alternating 'tubes' that are strongly confined to near the surface, roughly on the Stokes-drift decay scale $(2k)^{-1} = 5$ m. The apparent tangential spacing between the tubes is somewhat shorter than between the zones

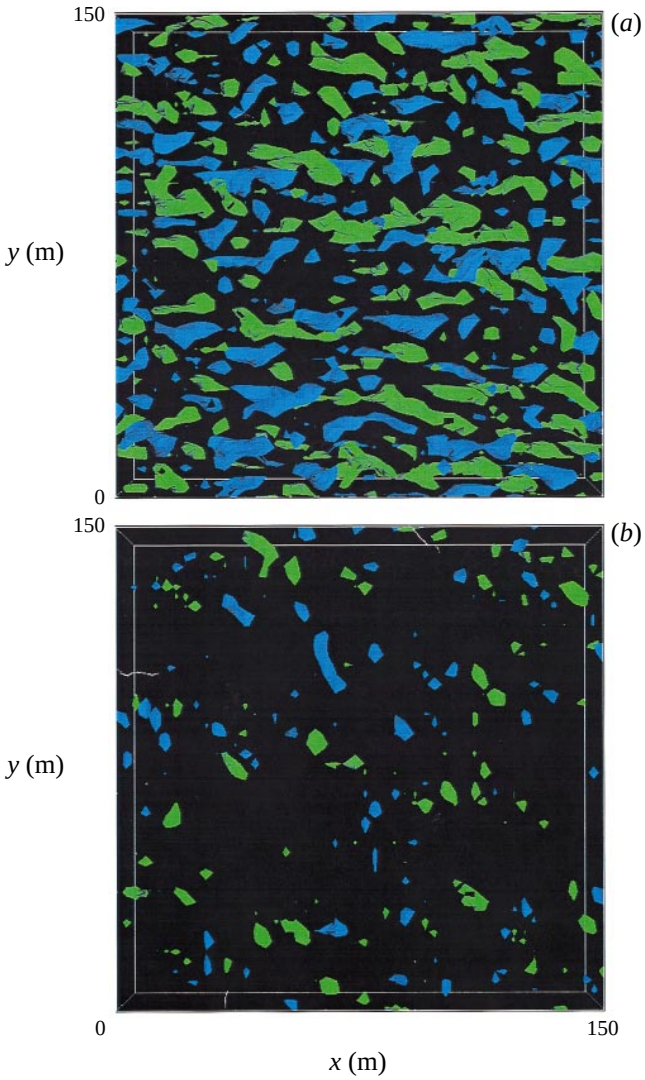

FIGURE 11. Instantaneous iso-surfaces of $\boldsymbol{\omega} \cdot \hat{\boldsymbol{x}}$ in (*a*) Langmuir turbulence (S/0.3) and (*b*) shear turbulence (S/∞) viewed from the top. The surface values are 0.017 (blue) and −0.017 (green).

in figure 10, and the direction of elongation is much more nearly due east than the east-southeast parcel motion within the convergence zones. In comparison with shear turbulence (figure 11*b*), the longitudinal vorticity in Langmuir turbulence is much stronger and more ordered into a longitudinal array.

Horizontal contour plots of instantaneous, near-surface vorticity and vertical velocity (figure 12*a*, *b*) confirm these impressions of smaller transverse spacing and primarily eastward orientation. The two fields are mutually aligned in the sense expected for roll cells; e.g. a tube of positive vorticity usually has an upwelling tube to the north and a downwelling tube to the south. On the other hand, the downwelling extrema and tubes are only moderately stronger and narrower than the upwelling ones, consistent with the only moderately negative skewness values near the surface (figure 7). Their width is clearly greater than that of the parcel density

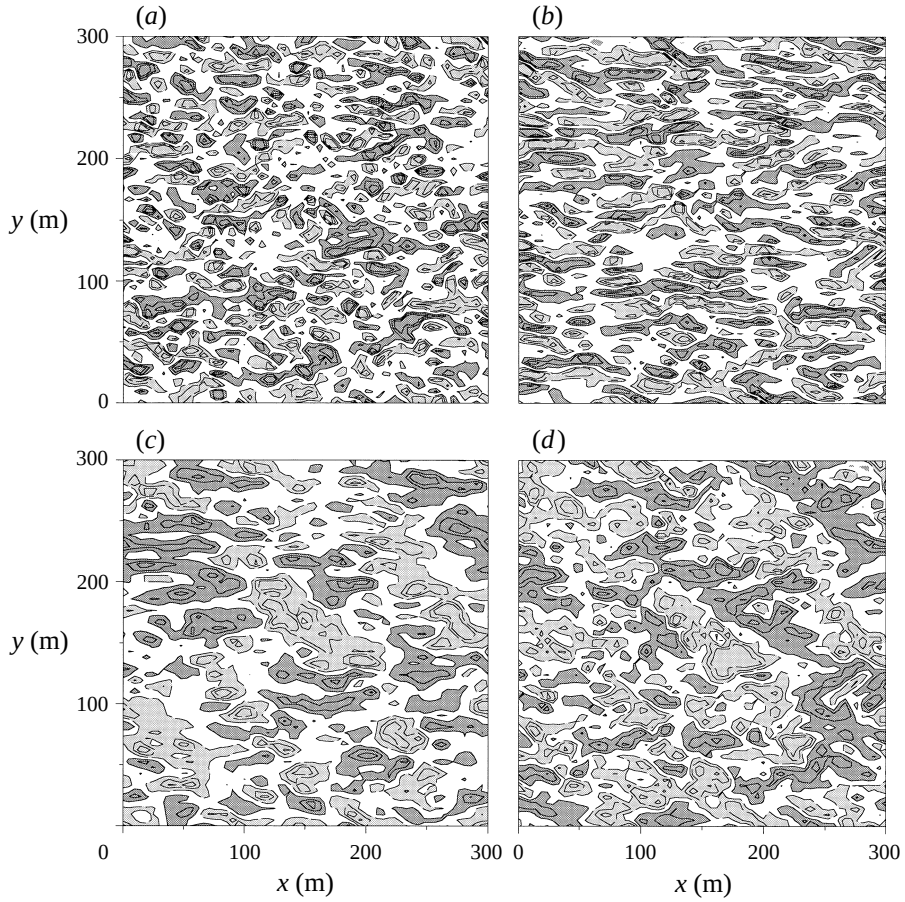

FIGURE 12. Horizontal contour plots of instantaneous (*a*) $\boldsymbol{\omega} \cdot \hat{\boldsymbol{x}}$, (*b*) w, (*c*) v', (*d*) u' in Langmuir turbulence (E/0.3). These fields are shown at $z = -3$ m, and the contour values for $\boldsymbol{\omega} \cdot \hat{\boldsymbol{x}}$ (in s^{-1}) and for w (in m s^{-1}) are (-0.015, -0.01, -0.005, 0.005, 0.01, 0.015) dark (light) shading are values larger (smaller) than 0.005 (-0.005). The contour values for u (in m s^{-1}) are (-0.015, -0.01, -0.004, 0.004, 0.01, 0.015) dark (light) shading are values larger (smaller) than 0.004 (-0.004); contour values for v (in m s^{-1}) are (-0.025, -0.015, -0.0060, 0.0060, 0.015, 0.025) dark (light) shading are values larger (smaller) than 0.006 (-0.006).

in convergence zones (figure 10). This width is also greater than in two-dimensional laminar Craik–Leibovich solutions, where it shrinks monotonically as $La_{lam} \rightarrow 0$ (Li & Garrett 1993). The longitudinal-transverse aspect ratio of the Langmuir cells is about 3 or 4, which is large but certainly not infinite (as in two dimensions).

The instantaneous horizontal patterns of near-surface horizontal velocity (figure 12*c*, *d*) are somewhat less well organized into roll-cell patterns: their horizontal aspect ratios are smaller than for vorticity and vertical velocity, especially for longitudinal velocity. Furthermore, the pattern orientation is somewhat more complex in that elongations are discernible both to the east on a smaller horizontal scale and to the southeast on a larger one. Nevertheless, their phase relations are roughly consistent with an idealized Langmuir cell: the v pattern shows tubes of convergence into the $w < 0$ tubes, and local maxima in u are in phase with minima in w. The pitch is defined as the ratio of the horizontally coincident u' maximum and w minimum, which occur at the surface and at about 5 m depth, respectively (see figure 6). From figures 12(*b*)

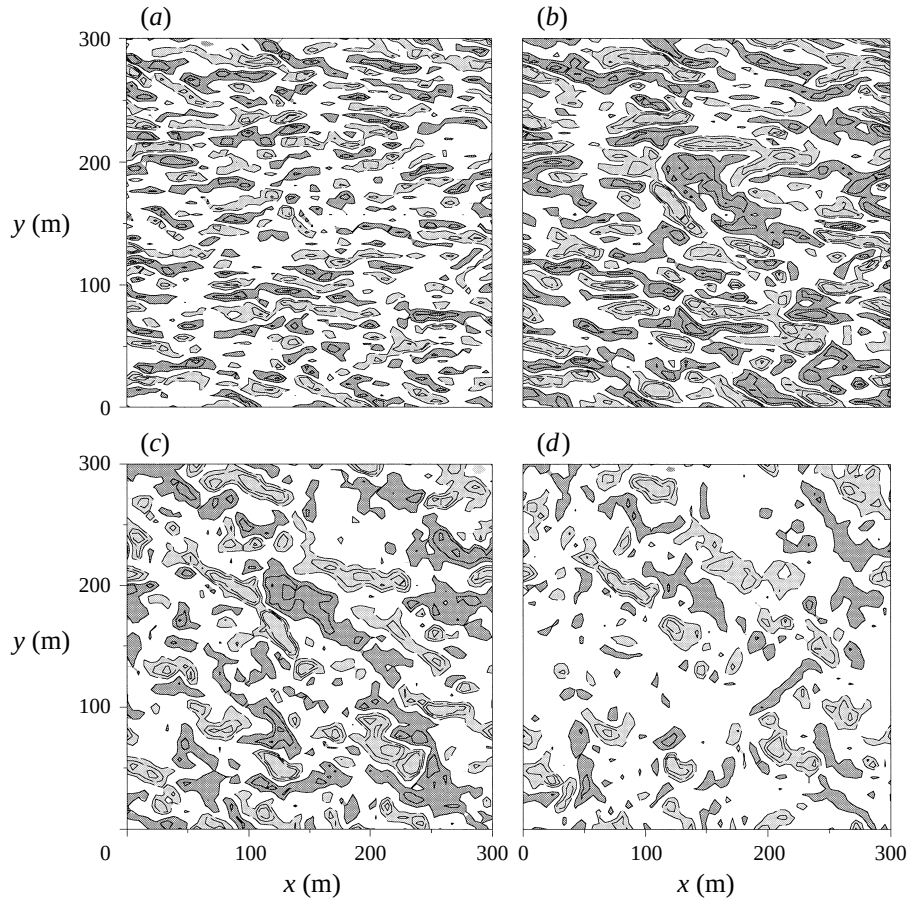

FIGURE 13. Horizontal contour plots of instantaneous w in Langmuir turbulence (E/0.3), averaged over different vertical intervals. Contour values (in m s^{-1}) are (-0.015, -0.01, -0.005, 0.005, 0.01, 0.015), dark (light) shading values larger (smaller) than 0.005 (-0.005). The averaging intervals (in m) are: (*a*) $-3 \geqslant z \leqslant 0$, (*b*) $-12 \leqslant z \leqslant -3$, (*c*) $-20 \leqslant z \leqslant -12$, and (*d*) $-30 \leqslant z \leqslant -20$.

and 12(*c*) it is evident that the pitch is of order unity for our turbulent Langmuir cell, roughly as observed by Weller & Price (1988) and also as in the Langmuir turbulence solutions of SD95 (their Plate 7). These values are much larger than the small pitch of two-dimensional laminar Langmuir cell for small La_{lam} (Li & Garrett 1993). The reason for this difference is primarily because two-dimensional Langmuir cell have narrow, strong downwelling zones beneath the surface convergence zones (proportional to $La_{lam}^{1/2}$ and $La_{lam}^{-1/3}$, respectively, as $La_{lam} \to 0$), whereas our and SD95's Langmuir turbulence solutions exhibit downwelling zones only about 30% narrower than the upwelling zones. In a two-dimensional solution, the instability to three-dimensional, turbulent motions does not occur, even as $La_{lam} \to 0$, and evidently the stirring by such motions keeps the downwelling zones broad.

The instantaneous circulation pattern changes with depth (figure 13). Near the surface the $w(x, y)$ tubes are longitudinally oriented with relatively small horizontal scales. With increasing depth, though, the direction of pattern elongation spirals clockwise towards a more diagonal orientation and the spatial scale expands. Also the asymmetry between stronger downwelling and weaker upwelling increases (as also

indicated by the increased skewness; figure 7). Very deep into the boundary layer, the tube-like pattern is more fragmented, suggesting that the degree to which Langmuir cells dominate the turbulent variability diminishes with depth. The Langmuir turbulence solutions of SD95 (their Plates 3 and 4) also show the scale expansion of $w(x, y)$ with depth, but not as much rotation of orientation as ours, consistent with their lack of a Stokes Coriolis force in the mean Ekman balance (§3).

In the presence of such a degree of irregularity, it is somewhat difficult to discern from a few examples what the typical Langmuir cell structure is. To educe this typical structure, we have made conditional averages in our Langmuir turbulence solutions. Since Langmuir cells are primarily identified by their strong downwelling sites underneath a surface convergence zone, we define the conditioning event $\mathscr{E}$ as all (x, y, t) instances of $w(x, y, z_*, t) \leqslant -w_*$, where w_* is the r.m.s w at the depth z_* where it is largest (i.e. about 5 m; see figure 6). Thus, the conditional average for a quantity P is defined by

$$\overline{P}(x', y', z') \equiv \langle P(x + x', y + y', z', t) | \mathscr{E} \rangle. \tag{6.2}$$

Of course, we could use alternative definitions of $\mathscr{E}$, such as one with a different value of w_* or one based upon a strong extremum in longitudinal vorticity; we have done some experimentation with these choices and not found a strong sensitivity in the shape of the resulting $\overline{P}$. Nevertheless, we appreciate the potential danger of circularity in educing a flow structure by a conditional average based upon a prior conception of its form; however, insofar as structural forms emerge in the averages beyond those imposed in the conditioning definition, we view the danger as not severe. Detection of coherent structures from experimental and numerical databases using conditional averages like (6.2) is well established for a variety of flows (e.g. Adrian 1992; Adrian *et al.* 1989) and is closely related to the method of stochastic estimation developed by Adrian and Moin (1988). An important result from this experience is that, when the conditional fields are normalized by the threshold value in $\mathscr{E}$, they are found to be nearly independent of the conditioning threshold, suggesting a certain degree of universality for the conditionally sampled fields.

The conditionally averaged velocity field $\overline{\boldsymbol{v}'}$ is shown in three-dimensional perspective in figure 14. The downwelling tube and its neighbouring upwelling tubes are longitudinally elongated near the surface, but with depth the downwelling axis rotates clockwise towards the diagonal direction and expands in width. The transverse velocity $\overline{v'}$ has a combined longitudinally and diagonally oriented tube structure flanking the downwelling tube near the surface, but at deeper levels it changes into a diagonally oriented, unidirectional (southward) flow region. The longitudinal velocity $\overline{u'}$ is positive (eastward) at all depths above and below the downwelling origin for the conditional averaging, but near the surface it abruptly changes to a reverse (westward) flow to the east of the origin. This sign reversal of $\overline{u}$ near the origin means that $\partial\overline{u'}/\partial x < 0$ combines appreciably with $\partial\overline{v'}/\partial y < 0$ to balance the downwelling. Horizontal contour plots of $\overline{\boldsymbol{v}'}(x, y)$ (figures 15–16) demonstrate the weaker and more distant features of the typical Langmuir cells circulation pattern in Langmuir turbulence. In $\overline{w}(x, y)$ (figure 15), we see the neighbouring cells, closely packed near the surface and more widely spaced at depth. The horizontal flow (figure 16) is convergent above the downwelling extremum (near $z = z_*$) and divergent below, and the flow pattern changes quite substantially with depth in both orientation and horizontal scale. Thus, the Langmuir cells in Langmuir turbulence are more longitudinally oriented with finer horizontal scales near the surface and have a more diagonal orientation and larger scales in the PBL interior.

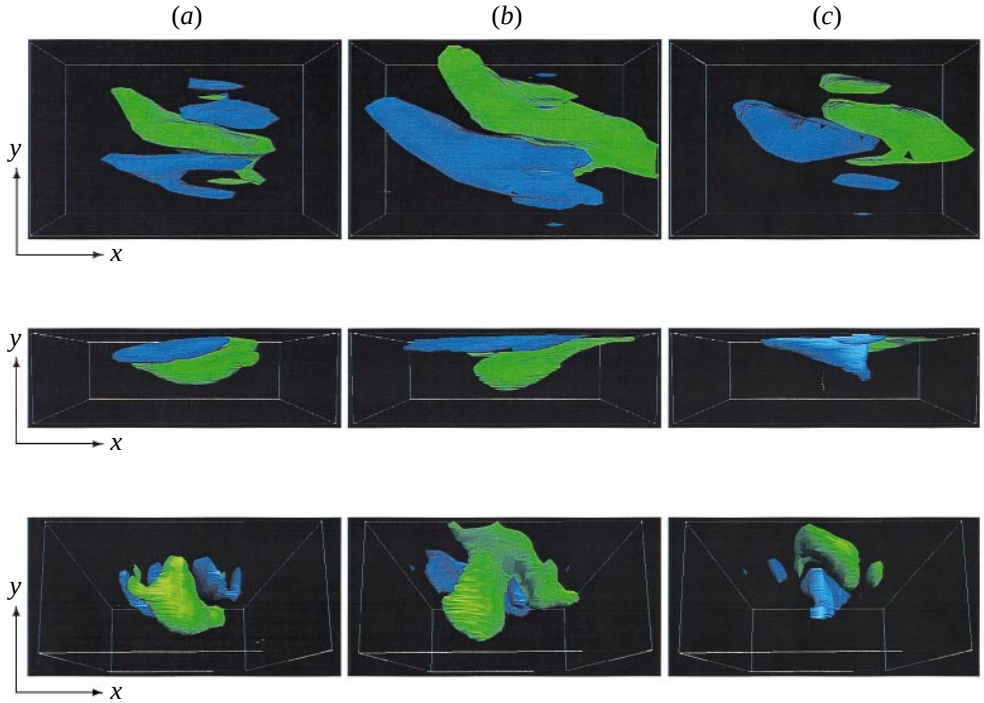

FIGURE 14. Iso-surfaces of conditionally averaged velocity: (*a*) $\overline{w}/U_*$, (*b*) $\overline{v'}/U_*$, and (*c*) $\overline{u'}/U_*$ in Langmuir turbulence (E/0.3. The three rows, respectively, are views from above, the south, and the east and below. Surface values are 0.19 (blue) and −0.19 (green) for all variables.

The conditionally averaged longitudinal vorticity (figure 17) exhibits a greater resemblance to idealized roll cells than do the other conditionally averaged fields. The Langmuir cell vorticity tubes are elongated in the longitudinal direction by a factor of more than five, relative to their transverse span. They alternate in sign, in an antisymmetric configuration about the conditioning origin, with strong intimations of transverse periodicity (i.e. a lattice-like array) over several periods. They are confined to near the upper surface; the deepest extent of the surfaces in figure 17 is only about 12 m. There is an evident longitudinal asymmetry, with an upward slant of the tube axis towards the surface in the down-wind direction; this asymmetry is analogous to the tilt of the hairpin vortices in shear turbulence (Head & Bandyopadhyay, 1981).

The conditionally averaged eddy flux densities (figure 18) show the local contributions of a Langmuir cell near the origin and asymptotically approach the domain-average profiles in the far field (cf. figure 3). The primary contribution to $\overline{u'w} < 0$ occurs in the core of the downwelling region in the upper 15 m, due to the coincidence of $u' > 0$ and $w < 0$ (figures 14*c* and 16). The broadest peak in $\overline{v'w} > 0$ lies deeper in the PBL, and it is associated with the $v' < 0$ region beneath the origin. Near the surface there are regions of both signs in this flux density that provide little spatially integrated net flux, consistent with vanishing near-surface flux in figure 3; these are associated with the different signs of both v' and w near the surface (figures 14*b* and 16). The normalized heat flux $Q_*^{-1}\ \overline{\theta' w}(z)$ has a positive extremum near the surface, that carries the surface buoyancy flux downward, and an opposite-sign extremum in the entrainment layer; the former is of relatively small horizontal extent, whereas the

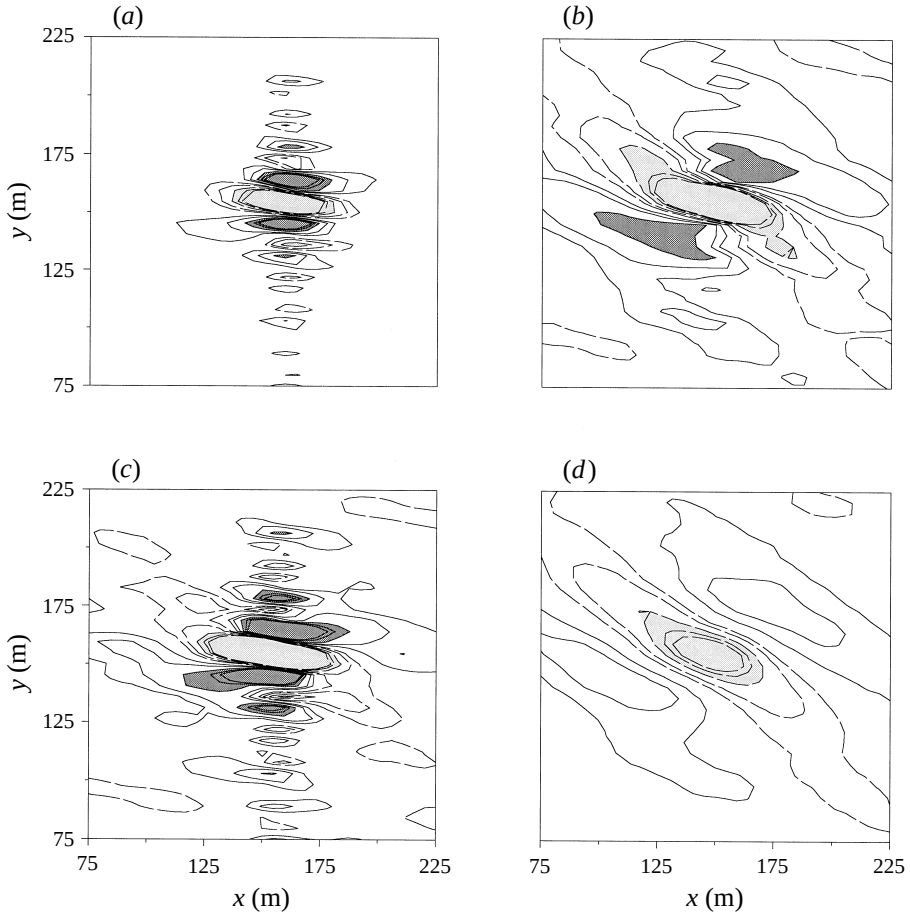

FIGURE 15. Contour plots of conditionally averaged vertical velocity $\overline{w}/U_*$ at different vertical levels in Langmuir turbulence (E/0.3): (*a*) $z = 1.2$ m, (*b*) $z = 4.8$ m, (*c*) $z = 12.0$ m, and (*d*) $z = 21.0$ m. Contour values are (−0.30, −0.25, −0.18, −0.10, −0.05, 0.050, 0.10, 0.18, 0.25, 0.3) dark (light) shading are values larger (smaller) than 0.18 (−0.18).

latter is much larger, consistent with the expanding scale of w with depth (cf. figures 13 and 15). This shows the efficiency of Langmuir cells in deeply penetrating the PBL for even a rather weak surface buoyancy flux, as has also been observed (Pollard & Thomas 1989). Because the local deviations in the flux magnitudes are substantial relative to the far-field values, it is clear that the Langmuir cells dominate the mean eddy transports in Langmuir turbulence: if we volume-average the conditionally averaged flux over the region in which it appreciably differs from its far-field value, we approximately recover the mean profiles in figures 3 and 8 (this is more precisely true for momentum than buoyancy).

7. Life cycles of turbulent Langmuir cells

A view of the temporal evolution of Langmuir cells is provided by the Hovmuller diagram in figure 19. As in the Lagrangian surface trajectories (figure 10), there is a prevailing southward motion in the patterns of w, but here the speed is somewhat smaller, around 0.025 m s^{-1}. The relevant advecting velocity for the vorticity field, as

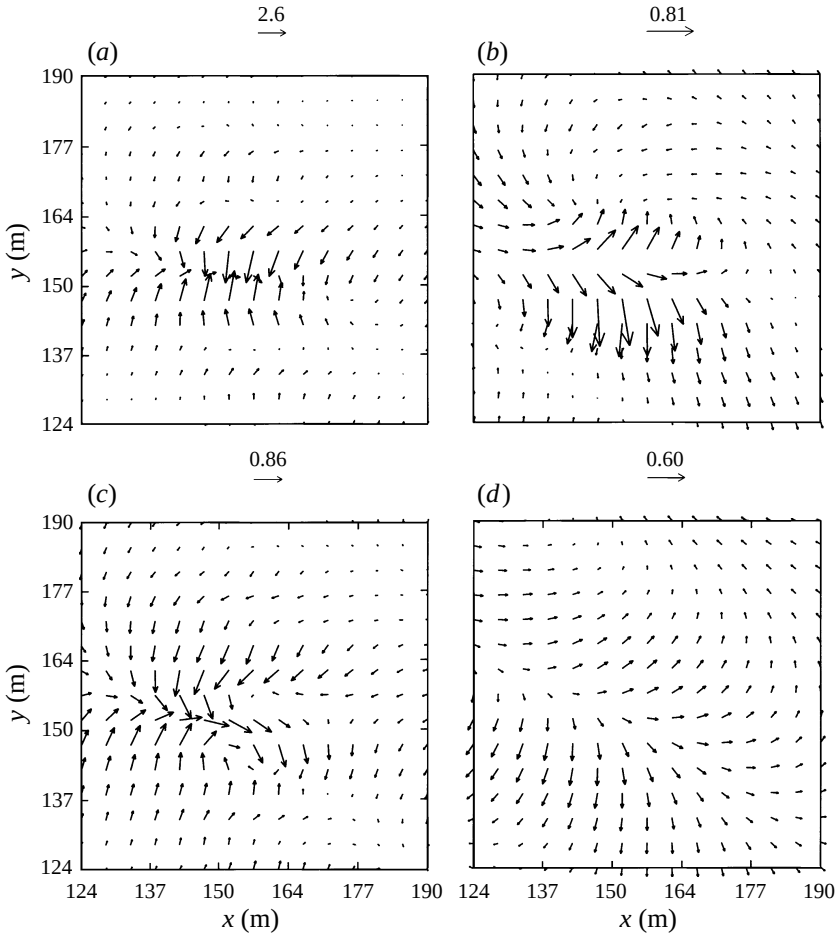

FIGURE 16. Vector plots of conditionally averaged horizontal velocity $\overline{\boldsymbol{v}'}/U_*$ at different vertical levels in Langmuir turbulence (E/0.3): (*a*) $z = 1.2$ m, (*b*) $z = 4.8$ m, (*c*) $z = 12.0$ m, and (*d*) $z = 21.0$ m. The vector length scales are indicated above each panel in m s^{-1}.

for tracers, is $\boldsymbol{v} + \boldsymbol{u}_S$ from (2.1), so only the Eulerian component, v, contributes to the y motion in figure 19, and its mean value in the middle of the boundary layer (figure 2) matches this pattern speed fairly well.

A given downwelling zone near $z = z_*$ in figure 19(*a*) waxes and wanes in strength and width over intervals of $O(10^3)$ s, comparable to the large-eddy turnover time. Many zones, particularly the stronger ones, have a lifetime of at least many turnover times. Even those that weaken and seem to disappear over a shorter interval are often replaced by successors occupying the same (advectively extrapolated) site. There are many examples here of Y-junctions of downwelling zones, more so than in instantaneous plots of spatial structure (i.e. figures 11 and 12; see also Thorpe 1992, and Farmer & Li 1995). Interestingly, the bases of the Y's all point to the future, indicating that zones tend to join each other rather than separate. Also the bases of the Y's are stronger and wider than the branches, indicating that joining provides a growth mechanism for the convergence zones. A time sequence in figure 20 illustrates the joining of two adjacent convergence lines, proceeding longitudinally away from an existing Y-junction by suppression of the longitudinal vortex pair

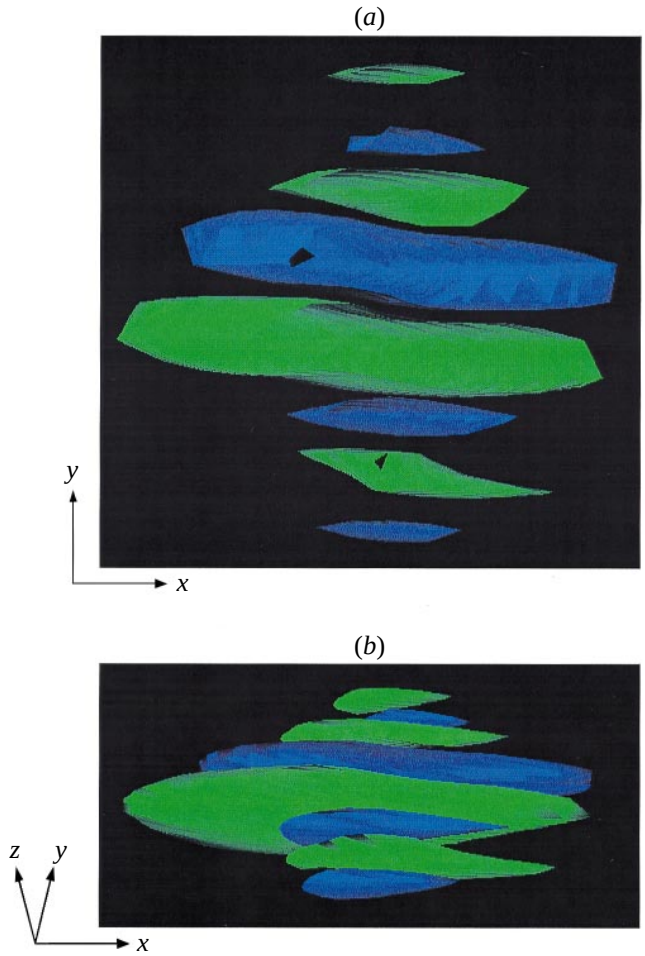

FIGURE 17. Iso-surfaces of conditionally averaged longitudinal vorticity, $\overline{\boldsymbol{\omega}} \cdot \hat{\boldsymbol{x}}$ normalized by U_*/z_i in Langmuir turbulence (E/0.3): (*a*) top view and (*b*) oblique perspective viewed from the side and from slightly above the water surface. Surface values are 5.0 (blue) and −5.0 (green).

initially lying between them. The longitudinal non-uniformities shown here differ from the two-dimensional Langmuir cell mergers calculated by Li & Garrett (1993), but the essential mechanism of vortex-pair suppression does seem to be the same. There may also be some dynamical similarity with the merger of like-sign vortices in homogeneous two-dimensional turbulence, which does not involve opposite-sign pair suppression (McWilliams 1984). In equilibrium, to balance a systematic reduction in the number of zones through joining, there is a continual regeneration of new, relatively weak and narrow zones, as well as the less frequent disappearance of some older, larger, previously joined zones.

The Hovmuller diagram for w deeper in the PBL (figure 19*b*) shows a similar bulk pattern motion. Its horizontal scale is larger, as expected from figures 13 and 15, and it has no unambiguous example of a Y-junction (although there is a hint of one near $t = 3000$ s, $y = 30$ m), indicating that the phenomena of zone merger and regeneration are much more common near the upper surface.

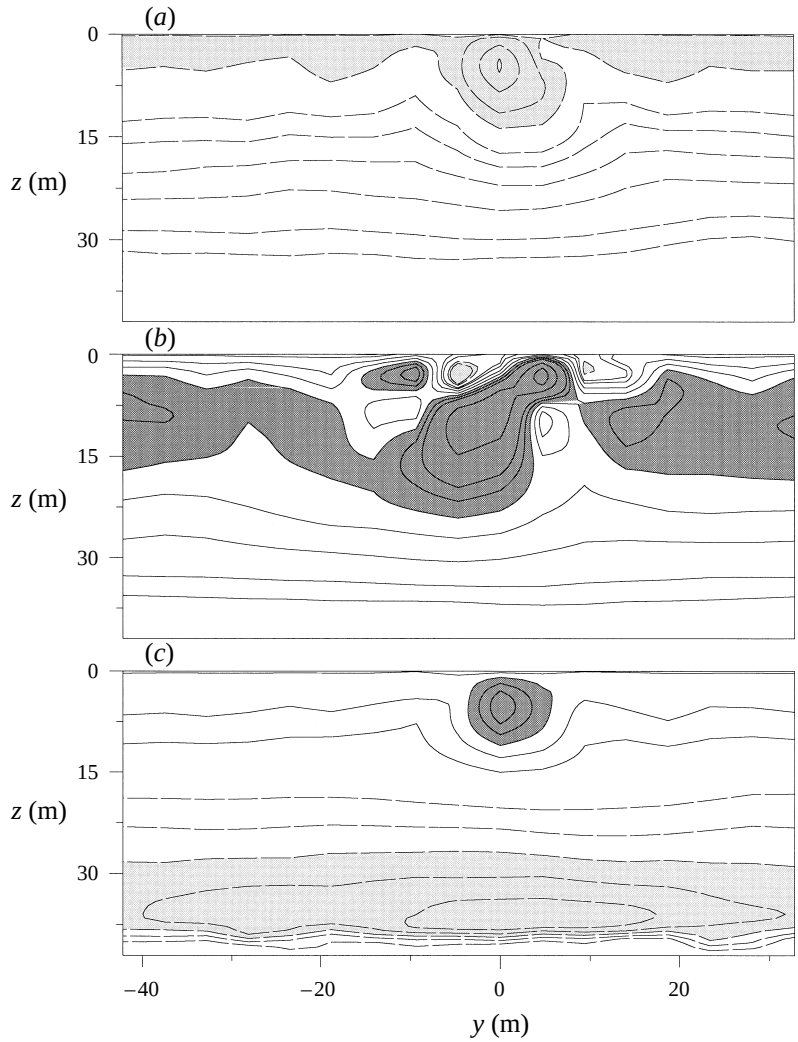

FIGURE 18. Transverse cross-sections of conditionally averaged momentum and heat fluxes in Langmuir turbulence (E/0.3). (*a*) $\overline{u'w}/U_*^2$ contours (−2.5, −2.0, −1.5, −1.0, −0.75, −0.5, −0.4, −0.3, −0.2, −0.1, −0.05, 0.05, 0.1), dark (light) shading values larger (smaller) than 0.05 (−0.75); (*b*) $\overline{v'w}/U_*^2$ contours (−0.1, −0.05, 0.05, 0.1, 0.2, 0.3, 0.4, 0.5, 0.6, 0.9, 1.2), dark (light) shading values larger (smaller) than 0.40, (−0.05); and (*c*) $\overline{\theta'w}/Q_*$ contours (−1.25, −1.0, −0.75, −0.5, −0.25, 0.25, 0.5, 0.75, 1.0, 1.25), dark (light) shading values larger (smaller) than 0.75 (−0.75).

8. Sensitivities

In the course of our research leading to the solutions analysed above, many other LES solutions were computed. It is not our present purpose to describe in detail the parameter dependences in Langmuir turbulence, but several qualitative results from this survey will be briefly reported.

The principal parameter of the problem posed in §4 is the turbulent Langmuir number La_{tur} defined in (1.1*b*). We have found, by varying U_s, that La_{tur} directly controls the strength of the differences between shear turbulence and Langmuir turbulence in the low-order statistical measures of the PBL (§5; figures 1–9). For

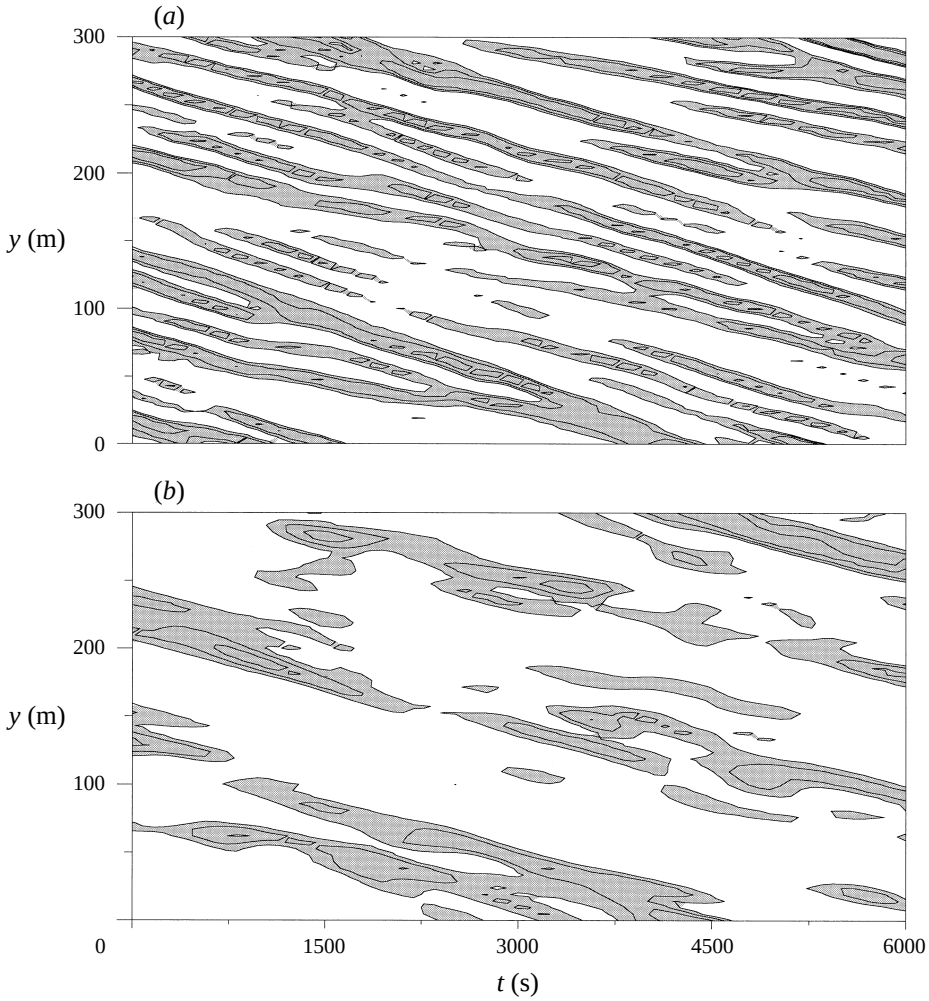

FIGURE 19. (y, t) phase diagram for instantaneous $w(0, y, \tilde{z}, t)$ in Langmuir turbulence (E/0.3) at (*a*) $\tilde{z} = -5$ and (*b*) $\tilde{z} = -20$ m. Downwelling contours (in m s^{-1}) are $(-0.016, -0.0080, -0.0020)$, shading indicates values below -0.002.

La_{tur} larger than about 0.5, these differences become rather small, which suggests that Langmuir cell may not be very important in equilibrium, wind-driven boundary layers with weak surface waves. Also, the degree of irregularity of the Langmuir cells strongly increases with La_{tur}. Variation of the gravity wavelength $2\pi/k$ alters the characteristic horizontal and near-surface vertical scales of the Langmuir cells roughly proportionally.

In an extreme case of $La_{tur} = 0$, achieved by setting the wind stress to zero, we find that $\boldsymbol{v} \approx -\boldsymbol{u}_s$ is an equilibrium LES solution with only weak turbulence. This flow has nearly zero total Coriolis force in (2.1), hence all other terms in the momentum balance can also be small; however, this state cannot be realized exactly because it is inconsistent with the surface-stress boundary condition. Evidently this flow configuration is a stable one, at least in our present LES implementation. This LES solution is unlike the laminar Stokes solution (3.11), because the effective (eddy) viscosity ν also becomes very small with weak turbulence.

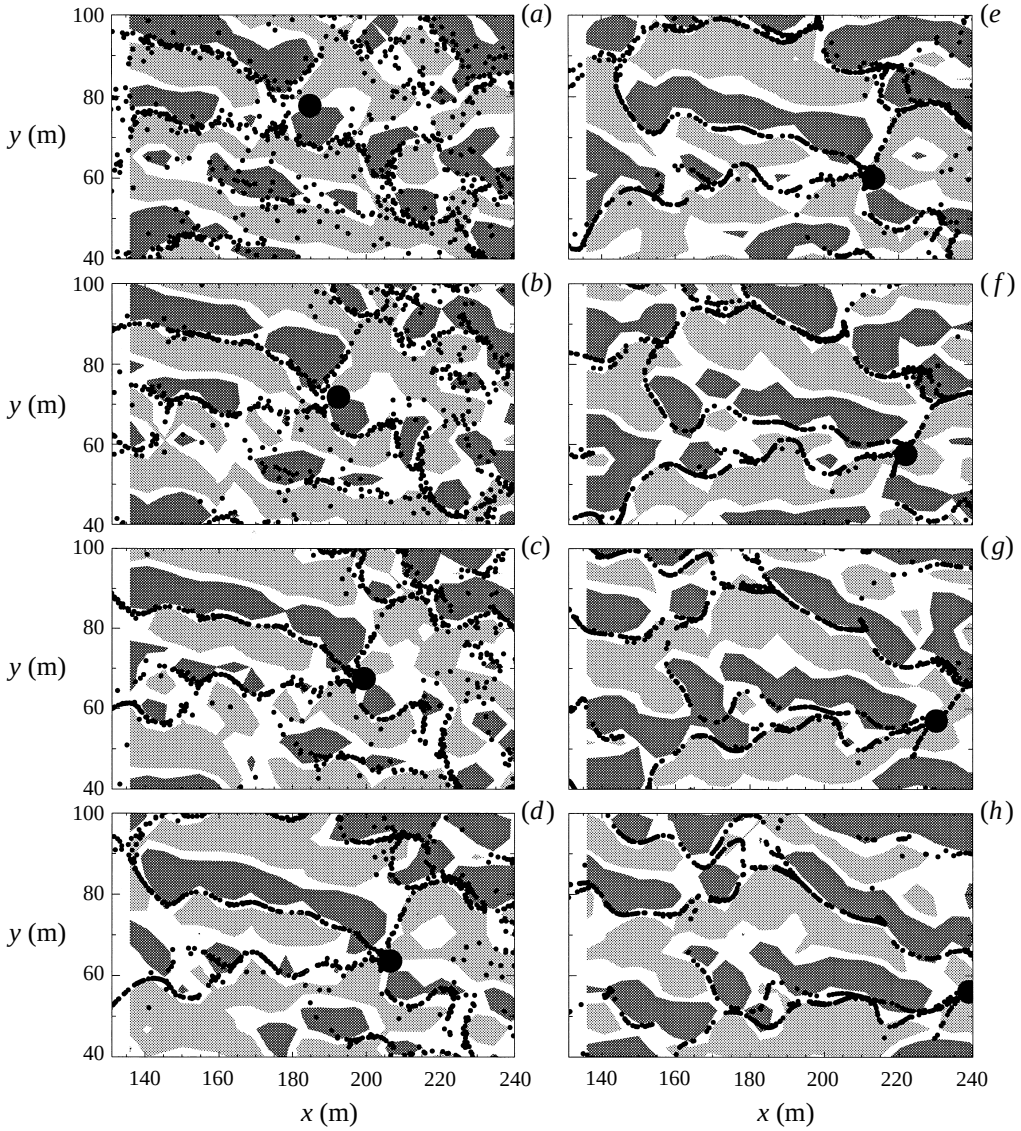

FIGURE 20. Temporal and spatial variation of surface particles and near-surface streamwise vorticity contours in Langmuir turbulence solution E/0.3 in the (x, y)-plane. Streamwise vorticity contours at level $z = -1.8$ m of magnitude (0.0055, -0.0055) s^{-1} are indicated by (dark, light) shading. Surface particles are denoted by small solid dots. The position of a single particle that is near the early-time Y-junction of two particle lines is indicated by large solid dot; note the Langmuir cell merger that occurs to the left of this particle. (*a–h*) Correspond to times [288, 448, 576, 704, 832, 992, 1120, 1248] s after the particles were randomly released.

Prompted by Li & Garrett (1995), we also have examined the influence of Langmuir cells in a much more convective PBL regime, with $Q_* = -370$ W m^{-2}, $La_{tur} = 0.3$, $z_i/L = -10.2$, and all other parameters the same as in §4. This implies, in their nomenclature, a Hoenikker number, $Ho \equiv -2\alpha g Q_*/k U_s U_*^2$, of about 1.5, which is still within the regime they declare to be Langmuir cell dominated. Our solutions partially support this conclusion: the Langmuir turbulence velocity statistics are still clearly

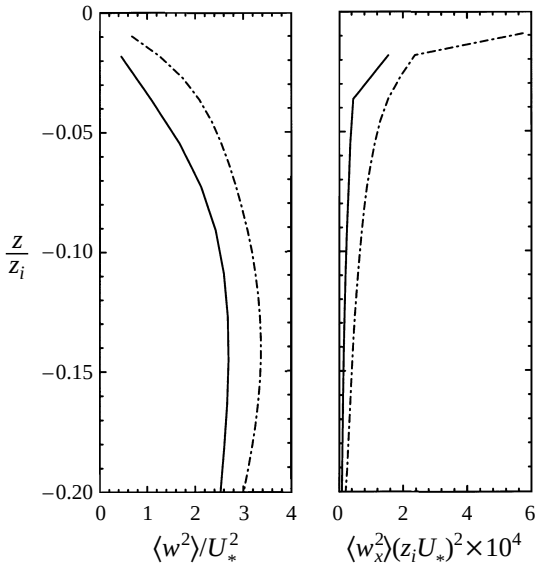

FIGURE 21. Vertical profiles in Langmuir turbulence solutions E/0.3 (solid line) and N/0.3 (dot-dash line) of $\langle w'^2\rangle(z)$, normalized by U_*^2, and $\langle(\boldsymbol{\omega}\cdot\hat{\boldsymbol{x}})^2\rangle(z)$, normalized by $(U_*/z_i)^2$.

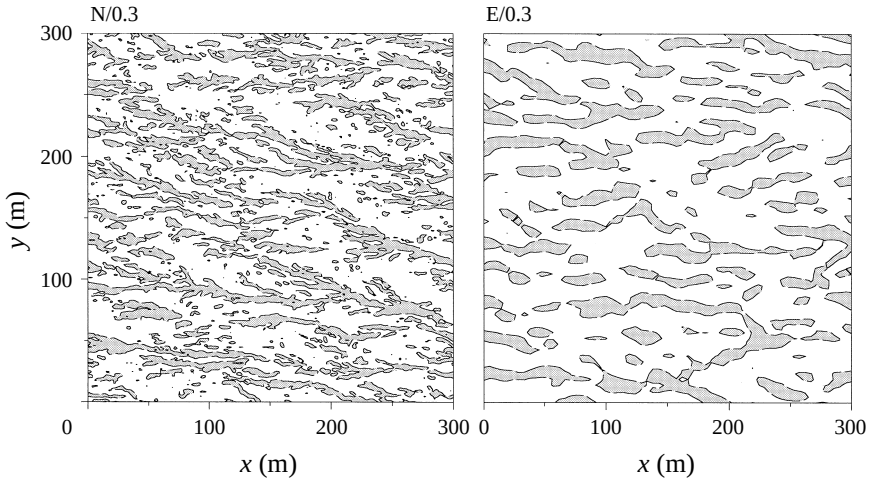

FIGURE 22. Instantaneous $w(x, y)$ at $z = -3$ m in Langmuir turbulence solutions E/0.3 and N/0.3. Values less than -0.005 m s^{-1} are shaded.

distinguishable from those of shear turbulence, but the mean buoyancy flux profile, including its entrainment-layer extremum, is nearly the same in both, which indicates that convective plumes have overcome Langmuir cells as the dominant flux-carrying mode. SD95 also found persistent Langmuir cell influences in strongly convective PBLs.

We have also calculated a Langmuir turbulence solution N/0.3 with increased spatial resolution using a nesting technique (Sullivan *et al.* 1996), with the grid spacings listed in section 4. Comparisons of this solution with the solution E/0.3 with standard resolution (figures 21 and 22) show that the spatial scale of the solution becomes increasingly smaller approaching the top surface as the grid is

refined, with a corresponding increase in amplitude for w and especially for ω, in an apparently singular fashion (i.e. without any limit as $\Delta \to 0$; see figure 21). Obviously this is not a physically sensible limit both because the rigid-lid approximation is inappropriate very close to the surface and because we have neglected the enhanced turbulent mixing and dissipation due to breaking surface gravity waves near the surface (Melville 1996), that would act to limit the scale decrease. Notice that the downwelling pattern (figure 22) manifests its smaller scales by increased branching from the primary Langmuir cell zones; this appears as a hierarchy of Y-junctions.

9. Conclusions

We have examined the roles of Langmuir cells in the turbulent planetary boundary layer (PBL) in large-eddy simulation (LES) solutions with and without the phase-averaged gravity-wave effects in the generalized Craik–Leibovich (Craik–Leibovich) equations. We find that, under typical wind and wave conditions, Langmuir turbulence with Langmuir cells can have significantly altered mean velocity and momentum flux profiles, greater anisotropy, and enhanced turbulent velocity variance and skewness, dissipation, and entrainment buoyancy flux, compared to shear turbulence without Langmuir cells. The characteristic flow structures in Langmuir turbulence do resemble somewhat the classical Langmuir cell solutions of the laminar Craik–Leibovich equations. However, they also exhibit considerable irregularity in space and time, and they have a rich structure with increasing depth, including scale expansion, rotation of Langmuir cell orientation, and transition from dipolar, horizontally converging u, v patterns to monopolar, momentum-fluxing patterns. There is no sharp separation of scales in Langmuir turbulence between the visually distinguisable Langmuir cell patterns and the even more irrregular motions on generally smaller scales. The horizontal structure has intermittent Y-junctions near the surface that occur on both the dominant Langmuir cell scale and finer ones. The Langmuir cells are also the primary flux transporting agents in Langmuir turbulence. Because of this, it is likely that PBL parameterization models need further development to adequately represent Langmuir turbulence effects, which act to increase the PBL transport efficiency when present, particularly the entrainment flux. Thus, the nature of the wind-driven oceanic PBL is determined by the relative strengths of the surface stress and the surface gravity-wave drift current, as measured by the turbulent Langmuir number La_{tur}.

The present solutions are only analysed during their equilibrium phase for the situation of steady, aligned wind and waves and negligible surface buoyancy flux. Obviously, typical oceanic conditions exhibit a much greater degree of transience than this and a wider range of buoyancy forcing. Also, our present formulation of the LES problem with a rigid lid for PBL motions and conservative Craik–Leibovich wave dynamics is inaccurate for small-scale motions near the surface. Thus, the subject of Langmuir turbulence provides a wide frontier for further exploration.

This research was supported by the Office of Naval Research and Minerals Management Service through contract N00014-92-F-0117 and by the National Science Foundation through the National Center for Atmospheric Research. We had helpful discussions with Darryl Holm and Sydney Leibovich in formulating this problem.

REFERENCES

Adrian, R. J. & Moin, P. 1988 Stochastic estimation of organized turbulent structure: homogeneous shear flow. *J. Fluid Mech.* **190**, 531–559.

Adrian, R. J. 1992 Stochastic estimation of conditional structure. *Eddy Structure Identification in Free Turbulent Shear Flows, IUTAM Symp., Poitiers, France.*

Adrian, R. J., Jones, B. G., Chung, M. K., Hassan, Y., Nithianandan, C. K. & Tung, A. T.-C. 1989 Approximation of turbulent conditional averages by stochastic estimation. *Phys. Fluids* A **6**, 992–998.

Anis, A. & Moum J. N. 1992 The superadiabatic surface layer of the ocean during convection. *J. Phys. Oceanogr.* **22**, 1221–1227.

Carruthers, D. J. & Moeng, C.-H. 1987 Waves in the overlying inversion of the convective boundary layer. *J. Atmos. Sci.* **44**, 1801–1808.

Coleman, G., Ferziger, J. & Spalart, P. 1990 A numerical study of the turbulent Ekman layer. *J. Fluid Mech.* **213**, 313–348.

Craik, A. D. D. & Leibovich, S. 1976 A rational model for Langmuir circulations. *J. Fluid Mech.* **73**, 401–426.

Craik, A. D. D. 1985 *Wave Interactions and Fluid Flows.* Cambridge University Press.

Farmer, D. M. & Li, M. 1995 Patterns of bubble clouds organized by Langmuir circulation. *J. Phys. Oceanogr.* **25**, 1426–1440.

Fernando, H. J. S. 1991 Turbulent mixing in stratified fluids. *Ann. Rev. Fluid Mech.* **23**, 455–493.

Head, R. M. & Bandyopadhyay, P. 1981 New aspects of turbulent boundary layer structure. *J. Fluid Mech.* **107**, 297–338.

Holm, D. D. 1996 The ideal Craik-Leibovich equations. *Physica* D **98**, 415–441.

Huang, N. E. 1979 On surface drift currents in the ocean. *J. Fluid Mech.* **91**, 191–208.

Klemp, J. & Duran, D. 1983 An upper boundary condition permitting internal gravity wave radiation in numerical mesoscale models. *Mon. Weather Rev.* **11**, 430–444.

Langmuir, I. 1938 Surface motion of water induced by wind. *Science* **87**, 119–123.

Large, W. G., McWilliams, J. C. & Doney, S. C. 1994 A vertical mixing scheme for momentum and buoyancy in an ocean model with a K-profile parameterization of the boundary layer. *Rev. Geophys.* **32**, 363–403.

Leibovich, S. 1980 On wave-current interaction theories of Langmuir circulations. *J. Fluid Mech.* **99**, 715–724.

Leibovich, S. 1983 The form and dynamics of Langmuir circulations. *Ann. Rev. Fluid Mech.* **15**, 391–427.

Leibovich, S. & Tandon, A. 1993 Three dimensional Langmuir circulation instability in a stratified layer. *J. Geophys. Res.* **98**, 16501–16507.

Lesieur, M. & Metais, O. 1996 New trends in large-eddy simulation of turbulence. *Ann. Rev. Fluid Mech.* **28**, 45–82.

Li, M. & Garrett, C. 1993 Cell merging and the jet/downwelling ratio in Langmuir circulations. *J. Mar. Res.* **51**, 737–769.

Li, M. & Garrett, C. 1995 Is Langmuir circulation driven by surface waves or surface cooling? *J. Phys. Oceanogr.* **25**, 64–76.

Li, M. & Garrett, C. 1997 Mixed-layer deepening due to Langmuir circulation. *J. Phys. Oceanogr.* **27**, 121–132.

Li, M., Zahariev, K. & Garrett, C. 1995 Role of Langmuir circualtion in the deepening of the ocean surface mixed layer. *Science* **270**, 1955–1957.

Magnaudet, J. & Thais, L. 1995 Turbulence structure below periodic surface waves. *Tenth Symposium on Turbulent Shear Flows, The Pennsylvania State University*, pp. 27/7–12.

McWilliams, J. C. 1984 The emergence of isolated, coherent vortices in turbulent flow. *J. Fluid Mech.* **146**, 21–43.

McWilliams, J. C., Gallacher, P. C., Moeng, C.-H. & Wyngaard, J. C. 1993 Modeling the oceanic planetary boundary layer. *Large-Eddy Simulations of Turbulent Flows*, pp. 441–454. Cambridge University Press.

Melville, W. K. 1996 The role of surface-wave breaking in air-sea interaction. *Ann. Rev. Fluid Mech.* **28**, 279–321.

Moeng, C.-H. 1984 A Large-Eddy-Simulation model for the study of planetary boundary-layer turbulence. *J. Atmos. Sci.* **41**, 2052–2062.

Phillips, O. M. 1977 *The Dynamics of the Upper Ocean*. Cambridge University Press.

Pollard, R. T. 1977 Observations and theories of Langmuir circulations and their role in near surface mixing. In *A Voyage of Discovery: George Deacon 70th Anniversary Volume* (ed. M. Angel), pp. 235–251.

Pollard, R. T. & Thomas, K. J. H. 1989 Vertical circulation revealed by diurnal heating of the upper ocean in late winter. Part I: observations. *J. Phys. Oceanogr.* **19**, 269–278.

Rotta, J. C. 1951 Statistiche theorie nichthomogener turbulens. *Z. Phys.* **129**, 547–572.

Skyllingstad, E. D. & Denbo, D. W. 1995 An ocean large-eddy simulation of Langmuir circulations and convection in the surface mixed layer. *J. Geophys. Res.* **100**, 8501–8522 (referred to herein as SD95).

Smith, J. 1992 Observed growth of Langmuir circulation. *J. Geophys. Res.* **97**, 5651–5664.

Sullivan, P. P., McWilliams, J. C. & Moeng, C.-H. 1994 A sub-grid-scale model for Large-Eddy Simulation of planetary boundary-layer flows. *Boundary-Layer Met.* **71**, 247–276.

Sullivan, P. P., McWilliams, J. C. & Moeng, C.-H. 1996 A grid-nesting method for large-eddy simulation of planetary boundary-layer flows. *Boundary-Layer Met.* **80**, 167–202.

Tandon, A. & Leibovich, S. 1995 Secondary instabilities in Langmuir circulations. *J. Phys. Oceanogr.* **25**, 1206–1217.

Thorpe, S. 1984 The effect of Langmuir circulation on the distribution of submerged bubbles caused by breaking waves. *J. Fluid Mech.* **142**, 151–170.

Thorpe, S. 1992 The break-up of Langmuir circulation and the instability of an array of vortices. *J. Phys. Oceanogr.* **22**, 350–360.

Weller, R. A. & Price, J. F. 1988 Langmuir circulation within the oceanic mixed layer. *Deep-Sea Res.* **35**, 711–747.

Wyngaard, J. C., Cote, O. R. & Izumi Y. 1971 Local free convection, similarity, and the budges of shear stress and heat flux. *J. Atmos. Sci.* **28**, 1171–1182.

Zedel, L. & Farmer, D. M. 1991 Organized structures in subsurface bubble clouds: Langmuir circulation in the open ocean. *J. Geophys. Res.* **96**, 8889–8900.